Coupled Numerical Scheme for Vascular Fluid-Tube Interaction using Large Deformation Theory. Application to Aneurysm Dynamics under Pulsatile Flow

Hamzah Bakhti, Lahcen Azrar, Mahmoud Hamadiche

Coupled Numerical Scheme for Vascular Fluid-Tube Interaction using Large Deformation Theory.

Application to Aneurysm Dynamics under Pulsatile Flow

Hamzah Bakhti · Lahcen Azrar · Mahmoud Hamadiche

Abstract A methodological approach is elaborated to study the vascular fluid-tube interaction under pulsatile blood flow within an asymmetrical nonlinear aneurysm and large deformation models. The aneurysm dynamics were modeled using a simplified Lagrangian nonlinear system describing the arterial wall motion with large deformation. The flow is governed by the Navier-Stokes equations in two-dimensional domain. A semi-implicit splitting scheme coupled with the finite difference method is developed to solve the flow equation in an irregular domain using a mesh transformation. On the other hand, the wall equations are solved using the Runge-Kutta method combined with the shooting technique by reducing the resulted boundary value problem to an initial value problem. Rigid and elastic aneurysms are considered and the effect of various geometrical and fluid parameters on the flow are investigated, mainly the Reynolds number, the aneurysm length and height. The study focused on the effect of the asymmetric curvatures of the tube walls and their deformations due to the pulsatile flow. The flow is examined under a steady inlet flow as well as under a pulsatile one for various aneurysm forms. The obtained numerical results validate the fluid and structure solvers and demonstrate significant differences between the rigid and elastic models of the structure as well as the effect of the asymmetric propriety of the arterial aneurysm.

H. Bakhti
Research Center STIS, M2CS, Department of Applied Mathematics & Informatics, ENSET, Mohammed V University in Rabat, Morocco
E-mail: hamzah.bakhti@um5s.net.ma

L. Azrar
Research Center STIS, M2CS, Department of Applied Mathematics & Informatics, ENSET, Mohammed V University in Rabat, Morocco
Department of Mechanical Engineering, Faculty of Engineering, KAU, Jeddah, Saudi Arabia
E-mail: l.azrar@um5s.net.ma

M. Hamadiche
LMFA, Ecole Centrale de Lyon, 36 Avenue Guy de Collongue, 69134, Ecully, France
E-mail: mahmoud.hammadich@gmail.com

List of Symbols

(o, x, y)	Original frame
$\mathbf{u}(x, y) = (u, v)$	Fluid velocity
$p(x, y)$	Fluid pressure
(o, ξ, η)	Reference frame
$\mathbf{d}(\xi, \eta) = (d_1, d_2)^t$	Wall displacements
ρ	Fluid density
μ	Fluid viscosity
U	Reference velocity
R_0	Half width of the rigid artery
Re	Reynolds number
$\mathbf{F}$	Deformation gradient tensor
$\mathbf{e}$	Displacement gradient tensor
$\mathbf{E}$	Lagrangian finite strain tensor
$\mathbf{S}$	Second Piola-Kirchhoff tensor
$\lambda_s,\ \mu_s$	Lamé constants
$\mathbf{P}$	First Piola-Kirchhoff tensor
ρ_s	Mass density
$\mathbf{f}$	Body force
$P_{int},\ P_{ext}$	Internal and external pressures
$\mathbf{n}$	Outward normal
$u_i n$	Inlet velocity
p_0	Outlet pressure
$u_0,\ v_0$	Initial velocity
$w_u,\ w_l$	Displacements of the upper and lower elastic walls
Δt	Time step size
$\Delta \xi$	Space step size
T	Maximum time

1 Introduction

Fluid-structure interaction problem (FSI) occurs in many cases when clear deformations of a structure are caused by fluid flow near or around it [1–4]. Depending on the fluid flow and the properties of the structure's material, these deformations can be large or small [5,6]. For the case of large deformations, the flow field and the structure deformations affect each other in a bidirectional way. Thus, the problem should be treated as a coupled multiphysics analysis. However, when large deformations and large displacements are involved, careful analysis is needed to tackle the domain displacement and the associated nonlinear deformation. In general, the mathematical modeling of FSI problems using large deformation theory results in complex and nonlinear systems of equations that remain a challenge to many researchers for years.

To better understand some cardiovascular diseases, many numerical techniques for FSI models were developed to study blood flow behavior through different types of arteries. Particularly, with arterial aneurysms, the abnormal dilation of the arterial wall results in blood vessel wall weakness. This can be life threatening as it leads to a higher risk of an arterial wall rupture and a more common type is abdominal aortic aneurysms (AAA) [7,8]. By considering the blood flow to be pulsatile, the FSI models are favorable to understanding both the behavior of the blood and the dynamics of the arterial aneurysm [9]. However, the numerical techniques are usually time-consuming due to the complexity of vascular FSI models because of the coupling between the mechanobiology of the wall and the pulsatile blood velocity-pressure fields [10]. Therefore, the study of these models, especially in a large deformation domain with the appropriate inlet/outlet boundary conditions, and using time-saving numerical schemes is very useful to understand the dynamics of arterial aneurysm due to pulsatile blood flow.

The study of FSI models is of considerable importance and has direct implications for many industrial, engineering and medical problems. These models draw the attention of researchers for years and many scientific works were published studying a variety of phenomena with applications in various fields, such as pumps [11], heart valves [12], aerodynamic flutter [13], shock absorbers [14], turbines [15] and biomechanics [16–18]. The analytical solutions are almost impossible to obtain, except for rare cases where many simplifications are assumed to the problem [19,20]. Thus, many numerical procedures were developed for this matter [21–23]. Meanwhile, various FSI models were proposed using the large deformation theory, worth mentioning the work of Tian *et. al.* [24] in which they studied a three-dimensional FSI model involving a large deformation theory with applications in biological systems. Various other works are elaborated using the same theory, as presented in [25–27].

Many research works studying the blood flow in arteries are based on the assumption of rigid deformed walls. Bakhti *et. al.* [28,29] studied the steady and pulsatile blood velocity profile and the resulting shear stress on a rigid asymmetric stenosed tapered artery using different rheological blood models. Finol and Amon [30] studied pulsatile blood flow and hemodynamic stresses in arteries with the presence of two, axisymmetric and rigid wall aneurysms using the spectral element method. Later on, Finol *et al.* used a three-dimensional model of AAAs with a single, asymmetric and rigid aneurysm using the finite element method [31]. More recently, more realistic numerical studies on blood dynamics based on rigid wall models are elaborated in [32–38]. By considering the blood flow to be pulsatile, the FSI models are favorable for understanding both the behavior of the blood and the dynamics of the arterial aneurysm [39]. Worth mentioning the work of Hamadiche [40], where the dynamics of symmetrical aneurysms in large deformations domain due to pulsatile blood flow are studied.

However, due to the high computation costs (run time, required memory) and the mathematical complexity of the vascular FSI models for blood flow, the existing numerical techniques are difficult to code and need powerful

computing machines. For this matter, many numerical methods were used to study FSI models in blood flow problems by applying techniques such as semi-implicit approaches and splitting schemes to reduce the computation costs. Also, reduced models seem to be helpful [41–45]. Actually, the geometrical and fluid parameters, such as the model parameters of the arterial aneurysm and the flow Reynolds number, have a great effect on the stability and convergence of these numerical schemes and that is due to their nature (explicit, semi-implicite, etc...). There is still a large need for more improved numerical techniques for such FSI problems using large deformation theory that are in general challenging in term of the high complexity and strong nonlinearity of these types of problems.

In this paper a mathematical model describing the wall motion in the Lagrangian formulation and using the large deformations theory is formulated. This model leads to a system of nonlinear equations governing the wall motion coupled with the Navier-Stokes equations for the flow motion. An adaptive numerical scheme is presented to simulate the FSI model using multiple techniques, namely, the Runge-Kutta coupled with the shooting method to solve the structure equations. The finite difference method (FDM) with a mesh transformation technique is elaborated to solve the flow equation in a two-dimensional domain combined with a semi-implicit splitting scheme. Multiple numerical experiments and tests have been elaborated in order to validate the proposed numerical scheme. The effect of various fluid and structure variables on the physiological parameters such as fluid velocity, pressure and wall displacement are deeply investigated. Results are obtained from elaborated methodological approaches to investigate blood flow and using the proposed vascular FSI model by considering two non-symmetrical aneurysms.

The paper is organized as follows: In section 2, the governing equations for the fluid (Section 2.2) are introduced, the derivation of the structural model for the wall motion is then presented (Section 2.1) and both models are completed by the appropriate initial and the coupling boundary conditions (Section 2.3). In section 3, a semi-implicit numerical scheme is introduced for the FSI solver which couples the Runge-Kutta and shooting method for the structure solver (Section 3.1) with the FDM for the fluid solver using a mesh transformation technique (Section 3.2). In section 4, a series of numerical tests were proposed to validate the structure and fluid solvers with a given exact solution for the structural model (Section 4.1) and classical blood flow problems in rigid arteries with the presence of different types of arterial aneurysms (section 4.2). The results of an FSI problem is then presented by coupling the wall model with the fluid equations to study the blood behavior in elastic arteries with the presence of asymmetrical aneurysms in both artery walls using the proposed nonlinear structure model (section 4.3). Finally, the main observations and results are given in the conclusion.

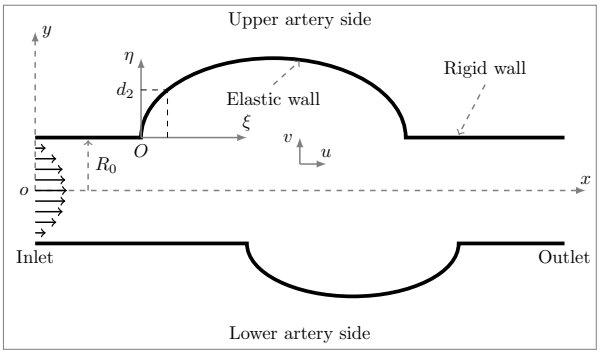

Fig. 1: Schematic representation of the fluid flow domain with defomable walls.

2 Mathematical Formulation

For the purpose of this paper, the flow of an incompressible Newtonian fluid in a two dimensional domain defined by a channel with both rigid and elastic parts of the parallel walls, as shown in Figure 1, is considered. The wall is assumed to be an incompressible continuum and its displacement is observed in the two dimensional reference frame (o, ξ, η).

Let d_1 and d_2 be the Lagrangian variables that relate the deformed configuration with the reference configuration of the wall and $\mathbf{d}(\xi, \eta) = (d_1, d_2)^t$ be the displacements vector of a particle in the continuum body.

On the other hand, u and v donate the velocities of the fluid in the x and y directions, respectively. $\mathbf{x}$ denotes the vector position of a point in the original frame (o, x, y), which is considered as an orthonormal basis where a two-dimensional flow of an incompressible and viscous fluid takes place in the (x, y)-plane.

A mathematical modeling of the wall kinematics and the governing equations of motion are elaborated herein, as well as the resulting basic flow equations.

2.1 Fluid Flow equations

The flow parameters are assumed to depend on only two space variables, x, y. The fluid flow is governed by the two-dimensional nonlinear Navier-Stokes equations for an incompressible viscous Newtonian fluid. The continuity and momentum equations are given in a compact form as follow

- *Continuity equation*

$$\nabla.\mathbf{u} = 0 \tag{1}$$

- *Momentum equation*

$$\rho\left(\frac{\partial \mathbf{u}}{\partial t} + \mathbf{u}.\nabla\mathbf{u}\right) = -\nabla p + \mu\Delta\mathbf{u} \tag{2}$$

where ρ is the fluid density, $\mathbf{u}$ is the flow velocity, p is the pressure and μ is the fluid viscosity. The system of equations modeling the flow field is given in the following explicit form

$$\begin{cases} \dfrac{\partial u}{\partial x} + \dfrac{\partial v}{\partial y} = 0 \\ \rho\left(\dfrac{\partial u}{\partial t} + u\dfrac{\partial u}{\partial x} + v\dfrac{\partial u}{\partial y}\right) = -\dfrac{\partial p}{\partial x} + \mu\left(\dfrac{\partial^2 u}{\partial x^2} + \dfrac{\partial^2 u}{\partial y^2}\right) \\ \rho\left(\dfrac{\partial v}{\partial t} + u\dfrac{\partial v}{\partial x} + v\dfrac{\partial v}{\partial y}\right) = -\dfrac{\partial p}{\partial y} + \mu\left(\dfrac{\partial^2 v}{\partial x^2} + \dfrac{\partial^2 v}{\partial y^2}\right) \end{cases} \tag{3}$$

The non-dimensional Navier-Stokes equations can be obtained using the following dimensionless variables

$$x^* = \frac{x}{L},\ \mathbf{u}^* = \frac{\mathbf{u}}{R_0},\ t^* = \frac{t}{L/R_0},\ p^* = \frac{p}{\rho U^2} \tag{4}$$

where U is a reference velocity proportional to the maximum inlet velocity at the inlet of the channel, R_0 is the half-width of the rigid part of the artery. Substituting the scales, the non-dimensionalized equations after dropping the stars are obtained

$$\begin{cases} \dfrac{\partial u}{\partial x} + \dfrac{\partial v}{\partial y} = 0 \\ \dfrac{\partial u}{\partial t} + u\dfrac{\partial u}{\partial x} + v\dfrac{\partial u}{\partial y} = -\dfrac{\partial p}{\partial x} + \dfrac{1}{Re}\left(\dfrac{\partial^2 u}{\partial x^2} + \dfrac{\partial^2 u}{\partial y^2}\right) \\ \dfrac{\partial v}{\partial t} + u\dfrac{\partial v}{\partial x} + v\dfrac{\partial v}{\partial y} = -\dfrac{\partial p}{\partial y} + \dfrac{1}{Re}\left(\dfrac{\partial^2 v}{\partial x^2} + \dfrac{\partial^2 v}{\partial y^2}\right) \end{cases} \tag{5}$$

where $Re = \frac{\rho U R_0}{\mu}$ is the Reynolds number.

2.2 Structure equation

2.2.1 Lagrangian description of wall kinematics

Following the Lagrangian description of motion and denoting by $\mathbf{d}(\xi, t)$ the displacements vector that depends only on ξ and time t, the resulted deformation gradient tensor $\mathbf{F}$ can be calculated using the relation $\mathbf{F} = \mathbf{I} + \nabla\mathbf{d}$, that is

$$\mathbf{F} = \begin{pmatrix} 1 + \frac{\partial d_1}{\partial \xi} & 0 \\ \frac{\partial d_2}{\partial \xi} & 1 \end{pmatrix} \tag{6}$$

Following the assumption that the wall is an incompressible continuum, the deformation gradient must satisfy the condition $\det \mathbf{F} = 1$, thus $\frac{\partial d_1}{\partial \xi} = 0$. Then

$$\mathbf{F} = \begin{pmatrix} 1 & 0 \\ \frac{\partial d_2}{\partial \xi} & 1 \end{pmatrix} \tag{7}$$

The displacement gradient tensor is then $\mathbf{e} = \nabla \mathbf{d} = \mathbf{F} - \mathbf{I}$. For a large deformation domain, the Lagrangian finite strain tensor is defined as a function of the displacement gradient tensor

$$\mathbf{E} = \frac{1}{2}\left[\mathbf{e} + \mathbf{e}^t + \mathbf{e}^t\mathbf{e}\right] \tag{8}$$

Thus, using (7), one gets

$$\mathbf{E} = \frac{1}{2}\begin{pmatrix} \frac{\partial d_2}{\partial \xi}^2 & \frac{\partial d_2}{\partial \xi} \\ \frac{\partial d_2}{\partial \xi} & 0 \end{pmatrix} \tag{9}$$

The continuum is assumed to be a hyperelastic material, which is a special case of a Cauchy elastic material. The following St. Venant-Kirchhoff model is used

$$\mathbf{S} = \left[-p + \lambda_s \operatorname{Tr}(\mathbf{E})\right]\mathbf{I} + 2\mu_s\mathbf{E} \tag{10}$$

where $\mathbf{S}$ is the second Piola-Kirchhoff stress, p the hydrostatic pressure of the fluid, λ_s and μ_s are the structure Lamé constants. The first Piola-Kirchhoff tensor denoted by $\mathbf{P}$ is given by

$$\mathbf{P} = \mathbf{FS} = \mathbf{S} + \mathbf{eS} \tag{11}$$

which yields to

$$\mathbf{P} = \left[-p + \lambda_s \operatorname{Tr}\mathbf{E}\right]\mathbf{F} + 2\mu_s\mathbf{FE} \tag{12}$$

Using a matrix form, one gets

$$\mathbf{P} = \left(-p + \frac{\lambda_s}{2}\frac{\partial d_2}{\partial \xi}^2\right)\begin{pmatrix} 1 & 0 \\ \frac{\partial d_2}{\partial \xi} & 1 \end{pmatrix} + \mu_s\begin{pmatrix} \frac{\partial d_2}{\partial \xi}^2 & \frac{\partial d_2}{\partial \xi} \\ \frac{\partial d_2}{\partial \xi} + \frac{\partial d_2}{\partial \xi}^3 & \frac{\partial d_2}{\partial \xi}^2 \end{pmatrix} \tag{13}$$

2.2.2 Governing equations of wall motion

Let us assume that the continuum is subjected to a body force $\mathbf{f}$, and let $\mathbf{d}$ denotes the displacement vector, ρ_s the mass density in the reference frame. The governing equation of motion for a deformable continuum can be expressed as

$$\rho_s \frac{\partial^2 \mathbf{d}}{\partial t^2} = \nabla \cdot \mathbf{P} + \mathbf{f} \tag{14}$$

Let us denote by P_{int} the internal fluid pressure on both sides of the wall, obtained from the fluid equations, P_{ext} is a fixed external pressure applied

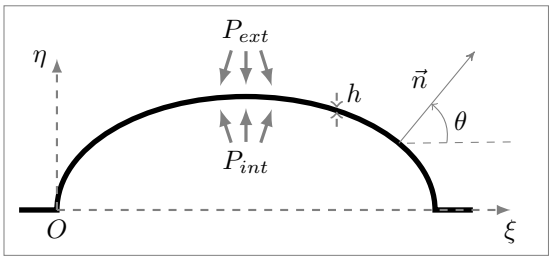

Fig. 2: Sketch of the body force applied on the wall.

on the outer tube wall and h is the wall thickness in the direction η of the reference frame. The body force can then be expressed as

$$\mathbf{f} = \frac{P_{int} - P_{ext}}{h}\mathbf{n} \tag{15}$$

where $\mathbf{n}$ is the outward normal to the wall as shown in Figure 2. For the wall that is defined implicitly by $\Gamma(\xi, \eta) = \eta - d_2(\xi) = 0$ the normal vector is then given by

$$\mathbf{n} = \frac{\nabla \Gamma}{\sqrt{\frac{\partial \Gamma}{\partial \xi}^2 + \frac{\partial \Gamma}{\partial \eta}^2}} = \begin{pmatrix} -\frac{\frac{\partial d_2}{\partial \xi}}{\sqrt{1+\frac{\partial d_2}{\partial \xi}^2}} \\ \frac{1}{\sqrt{1+\frac{\partial d_2}{\partial \xi}^2}} \end{pmatrix} \tag{16}$$

Thus, the explicit form of the body force, Eq. 15, is given by

$$\begin{cases} f_1 = -\dfrac{P_{int} - P_{ext}}{h} \dfrac{\frac{\partial d_2}{\partial \xi}}{\sqrt{1 + \frac{\partial d_2}{\partial \xi}^2}} \\ f_2 = \dfrac{P_{int} - P_{ext}}{h} \dfrac{1}{\sqrt{1 + \frac{\partial d_2}{\partial \xi}^2}} \end{cases} \tag{17}$$

The momentum equation in ξ-direction can be explicitly expressed as

$$\frac{\partial \left(-p + \left(\frac{\lambda_s}{2} + \mu_s \right) \frac{\partial d_2}{\partial \xi}^2 \right)}{\partial \xi} + f_1 = 0 \tag{18}$$

For the sake of condensed notations a new variable is defined as fellow

$$\phi = -p + \left(\frac{\lambda_s}{2} + \mu_s \right) \frac{\partial d_2}{\partial \xi}^2 \tag{19}$$

Using Eq.19, Eq. 18 reduces to

$$\frac{\partial \phi}{\partial \xi} - \frac{P_{int} - P_{ext}}{h} \frac{\frac{\partial d_2}{\partial \xi}}{\sqrt{1 + \frac{\partial d_2}{\partial \xi}^2}} = 0 \tag{20}$$

On the other direction η, the momentum equation is explicitly expressed as

$$\rho_s \frac{\partial^2 d_2}{\partial t^2} = \frac{\partial \left(\phi \frac{\partial d_2}{\partial \xi} \right)}{\partial \xi} + \mu_s \frac{\partial^2 d_2}{\partial \xi} + \frac{P_{int} - P_{ext}}{h} \frac{1}{\sqrt{1 + \frac{\partial d_2}{\partial \xi}^2}} \tag{21}$$

After further developments and using Eq. (20), one obtains

$$\rho_s \frac{\partial^2 d_2}{\partial t^2} = (\phi + \mu_s) \frac{\partial^2 d_2}{\partial \xi^2} + \frac{P_{int} - P_{ext}}{h} \sqrt{1 + \frac{\partial d_2}{\partial \xi}^2} \tag{22}$$

The final set of equations describing the elastic wall motion are thus given by

$$\begin{cases} \phi = -p + \left(\dfrac{\lambda_s}{2} + \mu_s \right) \dfrac{\partial d_2}{\partial \xi}^2 \\ \dfrac{\partial \phi}{\partial \xi} - \dfrac{P_{int} - P_{ext}}{h} \dfrac{\frac{\partial d_2}{\partial \xi}}{\sqrt{1 + \frac{\partial d_2}{\partial \xi}^2}} = 0 \\ \rho_s \dfrac{\partial^2 d_2}{\partial t^2} = (\phi + \mu_s) \dfrac{\partial^2 d_2}{\partial \xi^2} + \dfrac{P_{int} - P_{ext}}{h} \sqrt{1 + \dfrac{\partial d_2}{\partial \xi}^2} \end{cases} \tag{23}$$

In addition to the dimensionless fluid parameters given in (4), the following dimensionless structural parameters are used

$$\begin{aligned} &\xi^* = \frac{\xi}{R_0},\ h^* = \frac{h}{R_0},\ P^*_{int} = \frac{P_{int}}{\rho U^2}, \\ &P^*_{ext} = \frac{P_{int}}{\rho U^2},\ d_2^* = \frac{d_2}{R_0},\ \phi^* = \frac{\phi}{\rho U^2}, \\ &\rho_s^* = \frac{\rho_s}{\rho},\ \mu_s^* = \frac{\mu}{\rho U^2},\ \lambda_s^* = \frac{\lambda_s}{\rho U^2} \end{aligned} \tag{24}$$

The obtained dimensionless structural equations after dropping the stars are given by the same previous system of equations

$$\begin{cases} \phi = -p + \left(\dfrac{\lambda_s}{2} + \mu_s \right) \dfrac{\partial d_2}{\partial \xi}^2 \\ \dfrac{\partial \phi}{\partial \xi} - \dfrac{P_{int} - P_{ext}}{h} \dfrac{\frac{\partial d_2}{\partial \xi}}{\sqrt{1 + \frac{\partial d_2}{\partial \xi}^2}} = 0 \\ \rho_s \dfrac{\partial^2 d_2}{\partial t^2} = (\phi + \mu_s) \dfrac{\partial^2 d_2}{\partial \xi^2} + \dfrac{P_{int} - P_{ext}}{h} \sqrt{1 + \dfrac{\partial d_2}{\partial \xi}^2} \end{cases} \tag{25}$$

2.3 Initial and Boundary Conditions

The flow equations are completed by the appropriate inlet/outlet initial and boundary conditions. In this work, a periodic axial velocity profile at the inlet of the channel is considered and given by

$$u = u_{in}(y,t),\ v = 0 \text{ at the inlet} \tag{26}$$

where u_{in} is a known time-depended function to be introduced later. At the other end of the channel, the free outlet boundary condition is imposed as

$$\frac{\partial u}{\partial x} = \frac{\partial v}{\partial x} = 0,\ p = p_0 \text{ at the outlet} \tag{27}$$

where p_0 is the outlet pressure. On the channel wall the no-slip condition at the rigid solid wall and the continuity of the velocity at the elastic wall are assumed.

$$\begin{cases} u = v = 0 \text{ at the rigid wall} \\ u = 0,\ v = \dfrac{\partial d_2}{\partial t} \text{ at the wall} \end{cases} \tag{28}$$

For the initial conditions, a fixed velocity profile is assumed

$$u = u_0(x,y),\ v = v_0(x,y) \text{ at initial time } t_0 \tag{29}$$

where u_0 and v_0 are known functions to be defined later.

For the structural equations, both ends of the elastic curvature are assumed to be rigid, thus

$$d_2 = 0 \text{ at both ends of the elastic curvature} \tag{30}$$

3 Numerical Method

Numerical methodological approaches and a numerical code have been elaborated to solve the resulting fully coupled fluid and structure models. The code has been tested and several applications of the presented numerical method have been studied to ensure its effectiveness.

In the following subsections, the elaborated numerical techniques used to solve the resulting structural and fluid equations, as well as the algorithm of the FSI coupling, are presented. For the structural system, the coupling of the Runge-Kutta method with the shooting techniques is elaborated to switch the boundary value problem to an initial value one.

As for the flow equations, the FDM method is used to calculate the velocity-pressure fields in an irregular domain, where a mesh transformation technique that maps the complex flow domain into a regular one is used. For the time scheme, the pressure-correction method splitting the pressure from the velocity and reducing the CPU time is used. A forward finite differential scheme is then used to evaluate the time derivative.

3.1 Wall equations

The exterior pressure P_{ext} is supposed constant and once the interior pressure P_{int} is known, the structural system of equations can be solved using the Runge-Kutta method combined with the shooting technique. The time derivative is descritized using the following centered finite difference scheme

$$\frac{\partial d_2^{n+1}}{\partial t} \simeq \frac{d_2^{n+1} - 2d_2^n + d_2^{n-1}}{\Delta t^2} \tag{31}$$

The time-discretized wall equations are then expressed as

$$\begin{cases} \phi^{n+1} = -p + \left(\dfrac{\lambda_s}{2} + \mu_s\right) \dfrac{\partial {d_2^{n+1}}^2}{\partial \xi} \\ \dfrac{\partial \phi^{n+1}}{\partial \xi} - \dfrac{P_{int}^{n+1} - P_{ext}}{h} \dfrac{\frac{\partial d_2^{n+1}}{\partial \xi}}{\sqrt{1 + \frac{\partial {d_2^{n+1}}^2}{\partial \xi}}} = 0 \\ \rho_s \left(\dfrac{d_2^{n+1} - 2d_2^n + d_2^{n-1}}{\Delta t^2}\right) = \left(\phi^{n+1} + \mu_s\right) \dfrac{\partial^2 d_2^{n+1}}{\partial \xi^2} + \dfrac{P_{int}^{n+1} - P_{ext}}{h} \sqrt{1 + \dfrac{\partial {d_2^{n+1}}^2}{\partial \xi}} \end{cases} \tag{32}$$

which forms a system of equations to be solved as an initial value problem. Thus, the shooting technique is coupled to the Runge-Kutta method to solve the problem on the space variable ξ.

3.1.1 Shooting method

For the structure, one gets

$$\begin{cases} \dfrac{\partial \phi^{n+1}}{\partial \xi} = \dfrac{P_{int}^{n+1} - P_{ext}}{h} \dfrac{\frac{\partial d_2^{n+1}}{\partial \xi}}{\sqrt{1 + \frac{\partial {d_2^{n+1}}^2}{\partial \xi}}} = 0 \\ \dfrac{\partial^2 d_2^{n+1}}{\partial \xi^2} = \dfrac{1}{(\phi^{n+1} + \mu_s)} \left(\rho_s \left(\dfrac{d_2^{n+1} - 2d_2^n + d_2^{n-1}}{\Delta t^2}\right) - \dfrac{P_{int}^{n+1} - P_{ext}}{h} \sqrt{1 + \dfrac{\partial {d_2^{n+1}}^2}{\partial \xi}} \right) \end{cases} \tag{33}$$

For each time-step, one has the following boundary conditions of the structural displacement d_2

$$d_2(0) = 0, \ d_2(L_0) = 0 \tag{34}$$

where L_0 is the length of the elastic part of the wall. In order to transform the given boundary value problem to an initial value one, the missing initial value $\frac{\partial d_2}{\partial \xi}(0) = a$ is defined. Thus, the initial values are then

$$d_2(0) = 0,\ \frac{\partial d_2}{\partial \xi}(0) = a \tag{35}$$

The missing initial condition is obtained by finding the root of the function $F(a)$ defined as the value of d_2 at the second boundary using the initial value a

$$F(a) = d_2(L_0; a) \tag{36}$$

The Newton iteration is used to solve the root problem and the obtained value of a is then the corresponding initial value problem which then is also a solution of the boundary value problem.

3.2 Coupling with the flow equations

The Finite Difference Method (FDM) is used to solve the flow equations in a two-dimensional domain and the main difficulty is to apply the method to a complex geometry and with a moving boundary. To overcome this difficulty, the physical domain is mapped onto a rectangular one using the following coordinate transformation

$$\tau = t,\ x^* = x,\ y^* = \begin{cases} \dfrac{y}{R_0 + w_u} \text{ for } y \geq 0 \\ \dfrac{y}{R_0 - w_l} \text{ for } y < 0 \end{cases} \tag{37}$$

where w_u and w_l are, respectively, the displacement w_2 of the upper and lower elastic walls. The derivative rule is applied to compute all the derivatives involved in the Navier-Stokes equations, namely, for $y \geq 0$

$$\begin{cases} \dfrac{\partial}{\partial t} = \dfrac{\partial}{\partial \tau} - \dfrac{\partial w_u(x^*, \tau)}{\partial \tau} \left[R_0 + w_u(x^*, \tau)\right]^{-1} y^* \dfrac{\partial}{\partial y^*} \\ \dfrac{\partial}{\partial x} = \dfrac{\partial}{\partial x^*} - \dfrac{\partial w_u(x^*, \tau)}{\partial x^*} \left[R_0 + w_u(x^*, \tau)\right]^{-1} y^* \dfrac{\partial}{\partial y^*} \\ \dfrac{\partial}{\partial y} = \left[R_0 + w_u(x^*, \tau)\right]^{-1} \dfrac{\partial}{\partial y^*} \end{cases} \tag{38}$$

Similar expressions for the lower wall ($y < 0$) are used. The derivative rule can also be written in an analogous manner. Figure 3 shows an example of a mesh for the flow domain and for the rectangular one after using the given coordinate transformation.

The expressions of the new derivatives in the mapped domain are approximated using centered difference discretization, which is a second order

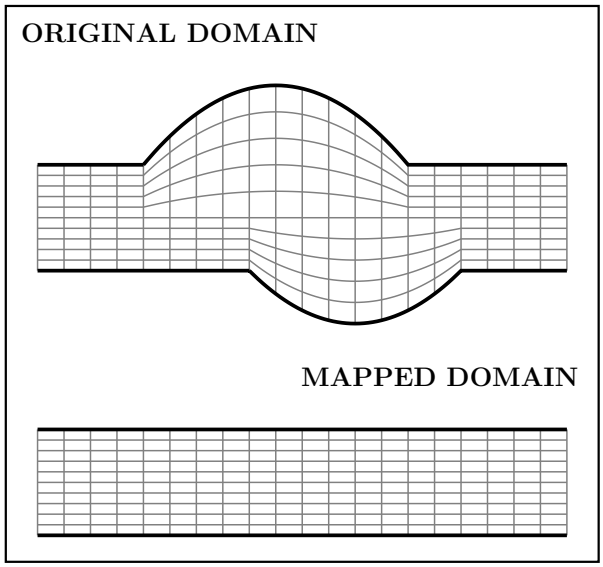

Fig. 3: Meshgrids of the original and mapped domains

approximation, for both first and second order derivatives and with respect to x and y, thus

$$\frac{\partial \mathbf{u}}{\partial x} \simeq \frac{\mathbf{u}_{i+1,j} - \mathbf{u}_{i-1,j}}{2\Delta x} \tag{39}$$

$$\frac{\partial \mathbf{u}}{\partial y} \simeq \frac{\mathbf{u}_{i,j+1} - \mathbf{u}_{i,j-1}}{2\Delta y} \tag{40}$$

$$\frac{\partial^2 \mathbf{u}}{\partial x^2} \simeq \frac{\mathbf{u}_{i+1,j} - 2\mathbf{u}_{i,j} + \mathbf{u}_{i-1,j}}{\Delta x^2} \tag{41}$$

$$\frac{\partial^2 \mathbf{u}}{\partial y^2} \simeq \frac{\mathbf{u}_{i,j+1} - 2\mathbf{u}_{i,j} + \mathbf{u}_{i,j-1}}{\Delta y^2} \tag{42}$$

A semi-implicit pressure-correction scheme (splitting method) is used to solve the two dimensional Navier-Stokes equations for incompressible fluid flow. A forward finite differential scheme is used to evaluate the time derivative. The predictor step is first done by solving the momentum equation without the pressure gradient term for a provisional velocity based on the previous outer loop one, namely,

$$\frac{\mathbf{u}^* - \mathbf{u}^n}{\Delta t} = -\mathbf{u}^n.\nabla \mathbf{u}^{n+1} + Re^{-1}\Delta \mathbf{u}^{n+1} \tag{43}$$

where $\mathbf{u}^*$ is the predictor velocity which is not divergence free. The viscosity term is treated implicitly while the convection term is treated semi-implicitly. The linear and nonlinear terms are evaluated using the second order central finite difference scheme. The second step is to correct the predictor velocity u^*,

such that the finally obtained velocity is divergence free. In order to maintain the Navier-Stokes equations as the basic flow equations, the pressure has to satisfy the following equation,

$$\frac{\mathbf{u}^{n+1} - \mathbf{u}^*}{\Delta t} = -\nabla p^{n+1} \tag{44}$$

The flow velocity is sought to be divergence free, i.e. $\nabla.\mathbf{u} = 0$, therefore, the pressure is obtained by solving the following Poisson equation

$$\nabla.\mathbf{u}^* = \Delta t \Delta p^{n+1} \tag{45}$$

This Poisson equation is solved with the following boundary conditions

$$\begin{cases} \dfrac{\partial p}{\partial x} = 0 \text{ at the inlet of the channel} \\ p = p_0 \text{ at the outlet of the channel} \\ n.\nabla p = 0 \text{ at the rigide and elastic wall} \end{cases} \tag{46}$$

The divergence free flow velocity can then be obtained from Eq. (44). Finally, the procedures followed to obtain the solution for the considered coupled fluid-structure models are presented in the following algorithm.

Fluid-Structure Interaction Algorithm

Define structural and fluid models parameters
Calculate the steady wall displacement
Generate initial fluid grids
Calculate the steady fluid solution
while $t \leq t_{max}$ **do**
  Calculate structure solution
  Upgrade fluid grids
  Calculate fluid solution
  $t = t + dt$
end while
Output FSI solution

4 Numerical Results

In this section, a series of numerical tests were proposed to validate the structure and fluid solvers with a given exact solution for the structural model and classical blood flow problems in rigid arteries with the presence of different types of arterial aneurysms. The results of an FSI problem is then presented by coupling the wall model with the fluid equations to study the blood behavior in elastic arteries with the presence of asymmetrical aneurysms in both artery walls using the proposed nonlinear structure model.

4.1 Validation of structure solver

In order to validate the numerical scheme used for the structure problem, an exact solution is introduced for the wall motion by adding new source terms f_1 and f_2 in the structure equation, Eq. (25), as follows

$$\begin{cases} \phi = -p + \left(\frac{\lambda_s}{2} + \mu_s\right) \frac{\partial d_2}{\partial \xi}^2 \\ \frac{\partial \phi}{\partial \xi} = \frac{P_{int} - P_{ext}}{h} \frac{\frac{\partial d_2}{\partial \xi}}{\sqrt{1 + \frac{\partial d_2}{\partial \xi}^2}} + f_1 \\ \frac{\partial^2 d_2}{\partial \xi^2} = \frac{1}{\phi + \mu_s} \left(\rho_s \frac{\partial^2 d_2}{\partial t^2} - \frac{P_{int} - P_{ext}}{h} \sqrt{1 + \frac{\partial d_2}{\partial \xi}^2} \right) + f_2 \end{cases} \tag{47}$$

The following structural components are considered

$$d_2(t, \xi) = \sin(\pi \xi) \frac{t^2}{2} \tag{48}$$

$$\phi(t, \xi) = -p + \left(\frac{\lambda_s}{2} + \mu_s\right) \frac{\partial d_2}{\partial \xi}^2 \tag{49}$$

Substituting the exact solutions in (47) and with simple calculations, the following source terms are obtained

$$f_1 = \frac{P_{int} - P_{ext}}{h} \frac{t^2 \pi \cos(\pi \xi)}{\sqrt{t^4 \pi^2 \cos(\pi \xi)^2 + 4}} - (\frac{t^4 \pi^3}{4} \sin(2\pi \xi)(\lambda_s/2 + \mu_s)) \tag{50}$$

$$\begin{aligned} f_2 = & \frac{-1}{\mu_s - p + \frac{t^4 \pi^2}{4} \cos(\pi \xi)^2 (\frac{\lambda_s}{2} + \mu_s)} \left(\rho_s \sin(\pi \xi) + \frac{P_{int} - P_{ext}}{h} \sqrt{\frac{t^4 \pi^2}{4} \cos(\pi \xi)^2 + 1} \right) \\ & - \frac{t^2 \pi^2}{2} \sin(\pi \xi) \end{aligned} \tag{51}$$

The convergence of the proposed numerical scheme is tested for the structural problem by computing the resulting error between the exact and numerically obtained solutions. The structure length is $L = 1$, the space discritization steps vary between $\Delta\xi = \{0.1, 0.05, 0.025, 0.0125\}$ and the maximum time is $T = 1$ while the time discitization step is a fixed value $\Delta t = 0.02$. The interior pressure is given by $P_{int} = 1 + 0.1 \cos(\xi)$. Table 1 presents the physical parameters used in the validation tests of the structure solver.

Figure 4 represents the comparison between the given exact solutions of d_2 and ϕ and the obtained numerical ones. It is clearly seen that the numerical solution converges to the exact one and is almost the same for the given physical parameters and the given values of the time step.

Table 1: Model parameters used in section 4.1.

Parameters	Values	Parameters	Values
L	1	T	1
ρ_s	0.1	λ_s	1000
μ_s	2000	h	0.1
p	10	P_{ext}	0.1

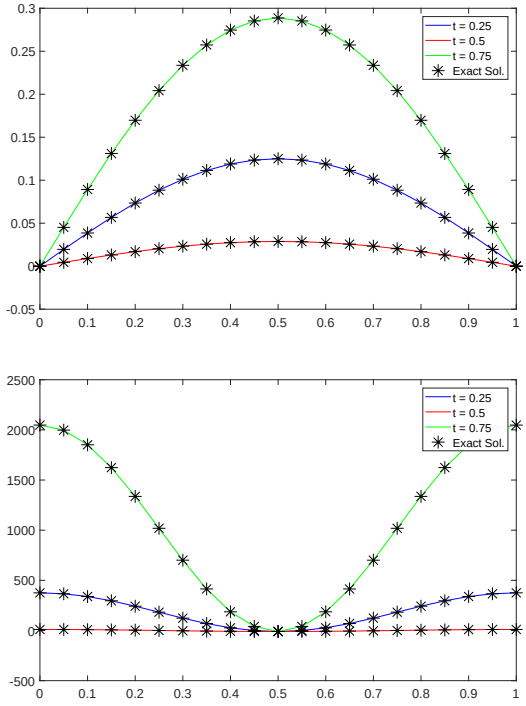

Fig. 4: Numerical and exact solution of the structure model for different values of t

Table 2 presents the resulting errors and rates of convergence of the numerical scheme for the structure model. The rate of convergence is calculated using $rate = \log_2 \frac{\|u_h - u\|_2}{\|u_{h/2} - u\|_2}$, where u_h is the numerical solution using the step h and u is the exact solution. The obtained results show that the numerical scheme is of the rate 1.5 in space for both d_2 and ϕ.

4.2 Validation of fluid solver

For the fluid solver validation, multiple computational experiments and tests in order to validate the proposed numerical scheme are presented. This is used

Table 2: Error analysis and the convergence rates of the structure solver for various $\Delta\xi$. Errors are calculated using the Euclidean norm and for $t = 0.5$

	d_2		ϕ	
$\Delta\xi$	$\|\tilde{d_2} - d_2\|_2$	rate	$\|\tilde{\phi} - \phi\|_2$	rate
2^{-1}	$3.0376531e-05$	-	$2.7657640e-01$	-
2^{-2}	$1.0065493e-05$	1.5935392	$8.8986147e-02$	1.6360254
2^{-3}	$3.4993314e-06$	1.5242667	$3.0507016e-02$	1.5444396
2^{-4}	$1.2319591e-06$	1.5061248	$1.0668136e-02$	1.5158329

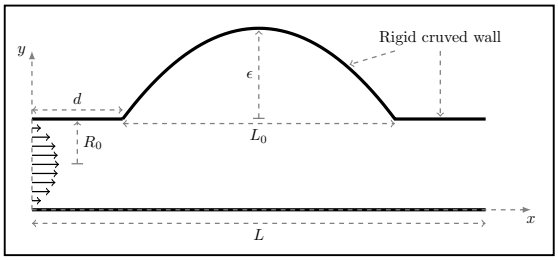

Fig. 5: 2D view of the geometry structure with a curvature at one side of the tube

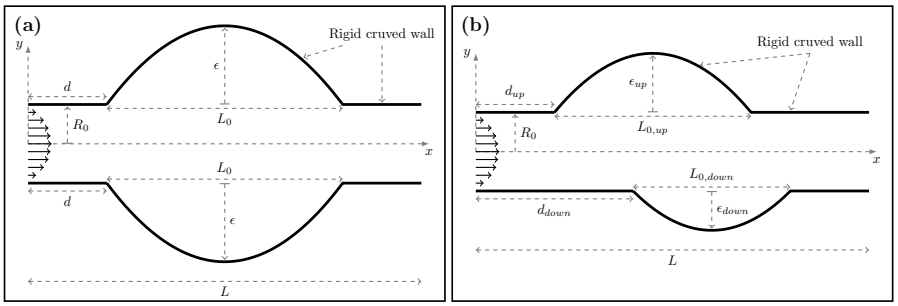

Fig. 6: 2D view of the geometry structure with symmetrical (a) and asymmetrical (b) curvatures at both sides of the tube

to examine the effect of various fluid variables on the physiological parameters such as fluid velocity and pressure. The obtained results are discussed and presented for two separate cases. In the first case considered below (Case 1), the fluid behavior in a rigid structure is studied with the existence of one curvature in a wall side of the tube (Figure 5) or multiple symmetrical or non-symmetrical curvatures at both sides of the tube (Figure 6), with the assumption of a steady fluid velocity at the inlet of the flow domain. Several numerical runs have been made and the obtained results are presented in three sub-cases (1a, 1b and 1c). The effects of fluid and structural parameters on the fluid flow are investigated.

In the second part (Case 2), the obtained results are presented and discussed for the case of rigid structure walls with asymmetrical curvatures at both sides of the tube (Figure 6b) and with the consideration of a pulsatile velocity at the inlet of the channel. The study focuses on the effect of the inlet pulse on the velocity field and fluid pressure in the flow domain.

4.2.1 Case 1 : Rigid wall with steady inlet

A simple fluid flow problem is considered in a tube with the presence of a curvature in the tube wall. The wall geometry functional for the case of a steady structure can be mathematically expressed, with modified inputs from [29], as follows

$$R(x) = \begin{cases} R_0 \left[1 + \frac{4\epsilon}{L_0^2}\left(L_0(x-d) - (x-d)^2\right)\right], & d \leq x \leq d + L_0 \\ R_0, & \text{otherwise} \end{cases} \tag{52}$$

where R_0 is the radius of the normal tube, L_0 is the curvature length, d indicates the location of the curvature and ϵ is the maximum height of the curvature outward the tube. This function is used for both upper and lower sides of the wall with various values of the used parameters. For the sake of clarity, this case is divided into three sub-cases in order to clarify the effects of different geometrical and fluid parameters on the flow field.

- Case 1a : Single wall curvature

In order to analyze the effect of the wall curvature on the fluid flow, a series of numerical runs were done with a rigid wall and a steady inlet flow. The wall geometry with the presence of one side deformed wall is shown in Figure 5. Therefore, on the rigid wall, the no-slip condition is assumed and the inlet function is defined without the unsteady part as follows

$$u_{in} = \frac{y}{R}\left(1 - \frac{y}{R}\right) \tag{53}$$

The geometric and mesh parameters, used in Case 1a, are given in Table 3. Numerical results were obtained using a regular grid, containing 51×51 fluid and pressure nodes. The time step used in the numerical tests is $\Delta t = 0.05$, which is well defined to assure the accuracy needed due to the splitting error. It is well-known that classical splitting schemes usually require smaller time step. The splitting method is used by separating the pressure and velocity differential operators and the main benefits of this scheme are the simple implementation and low computational costs.

On the other hand, the structural and fluid parameters are given in Table 4, where the exact curvature location, length and the maximum height that its can reach are given. Those values will be changed from case to case for a better understanding of the used model as well as the structural effect on the flow.

Figure 7 represents the fluid streamlines and the pressure contours in the steady regime for the given values in Table 4. It is observed from this figure

Table 3: Geometric and mesh parameters used in the Cases 1 and 2.

Parameters	Values	Parameters	Values
Initial time t_0	0	Final time T	50
Time step Δt	0.05	Normal Radius $R0$	0.5
Length of the channel L	10	Number of nodes ($Nx \times Ny$)	2601
x-Space step Δx	0.2	y-Space step Δy	0.02

Table 4: Structural and fluid parameters considered in case 1.

Parameters	Values
Reynold's number Re	200
Curvature location d	1
Curvature length L_0	4
Curvature max. height ϵ	1

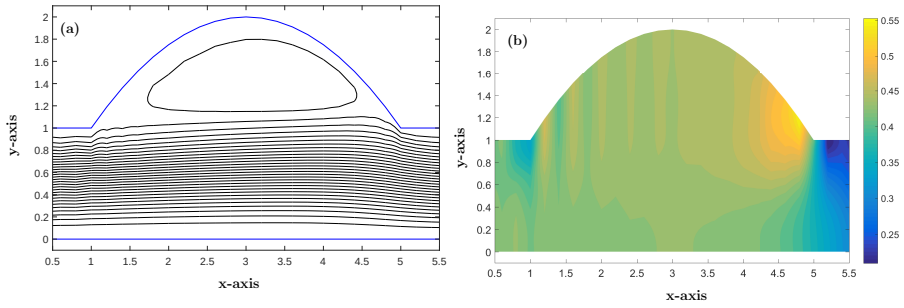

Fig. 7: Streamlines profile (a) and pressure contours (b) obtained in the steady regime for the case 1a

that the flow is uniform in the inlet zone and in the middle of the tube, while near the curved part of the wall it is clearly demonstrated that the flow forms a large roll that takes place in the entire deformed zone. On the other hand, the pressure contours, plotted in Figure 7b, show that a higher pressure occurs near the end of the deformed wall and slightly decreases around the deformed part of the wall toward the inlet.

Figures 8-11 illustrate the flow behavior and pressure evolution over time and streamlines variations for different values of Reynolds number (Re), curvature length (L_0) and the maximum height (ϵ). More precisely, Figure 8 represents the obtained streamlines at different time values, namely $t \in \{5,\ 10,\ 14.7,\ 25\}$, and for fixed values of the structural and fluid parameters given in Table 4. It is observed that the fluid streamlines begin as a uniform flow and rolls start to develop over time in the curved part of the tube and keep expanding and taking more space till it fill the full curved zone of the tube due to the increase of the fluid velocity until its maximum and the fluid flow reaches a steady regime.

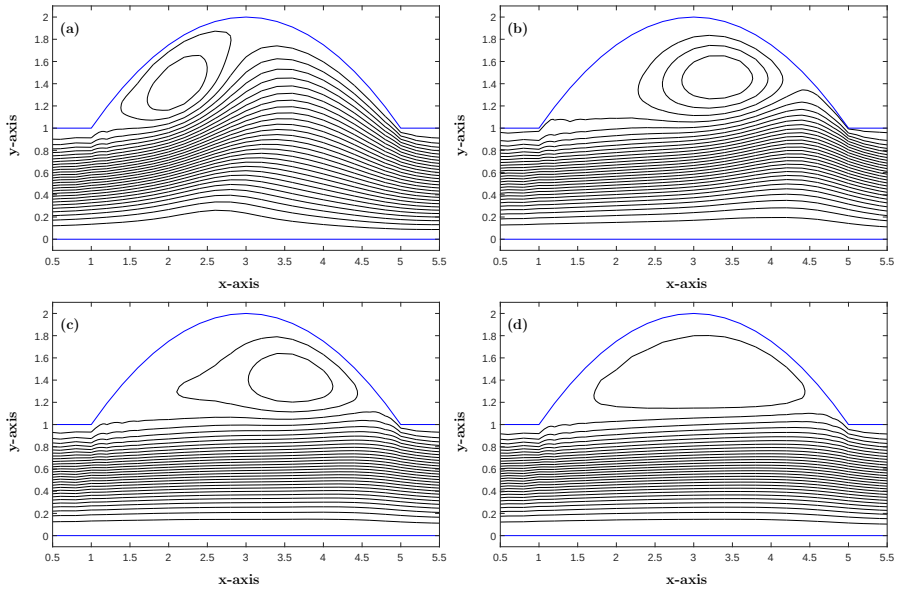

Fig. 8: Flow evolution corresponding to the Case 1a at different time values; (a) $t = 5$, (b) $t = 10$, (c) $t = 14.7$, (d) $t = 25$.

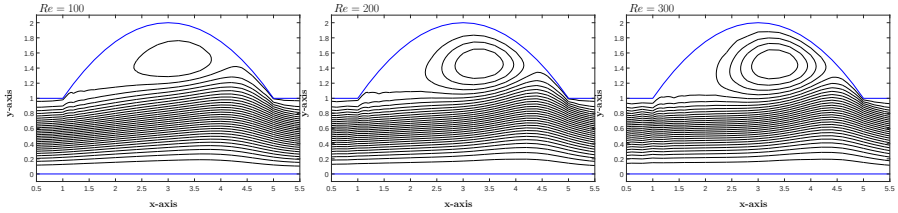

Fig. 9: Case 1a : Flow variation with respect to Reynolds number Re

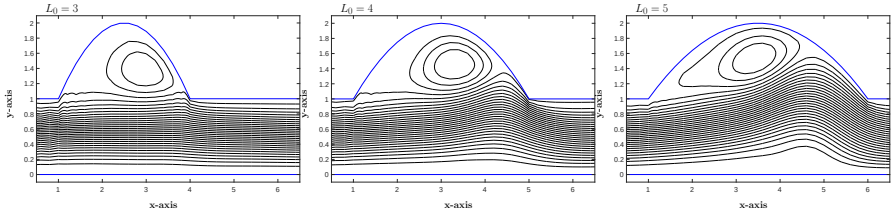

Fig. 10: Case 1a : Flow variation with respect to aneurysm length L_0

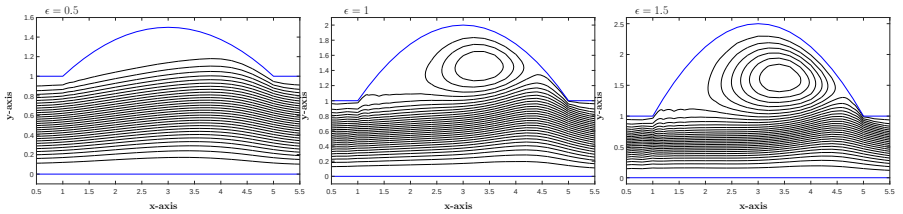

Fig. 11: Case 1a : Flow variation with respect to aneurysm maximum height ϵ

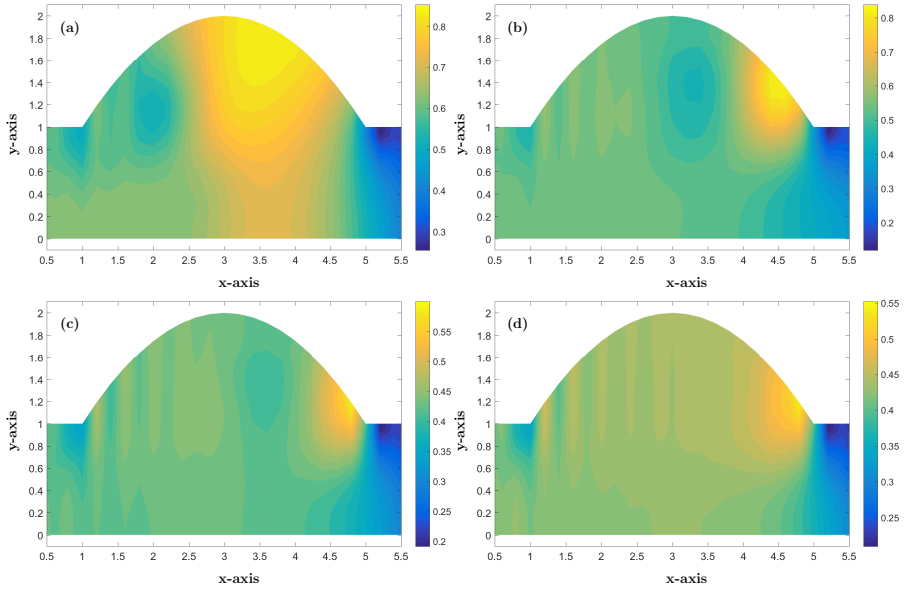

Fig. 12: Pressure contours corresponding to the Case 1a at different time values; (a) $t = 5$, (b) $t = 10$, (c) $t = 14.7$, (d) $t = 25$.

In Figure 12, the pressure evolution is presented over time, the pressure contours obtained in the same time interval as streamlines; $t \in \{5,\ 10,\ 14.7,\ 25\}$, and for the same fixed values of the structural and fluid parameters given in Table 4. It is observed from these results that a higher pressure occurs near the middle of the curvature and continues to move over time around the curvature heading to the end of the deformed wall. When the flow reaches the steady regime, the pressure takes a higher value near the end of the deformed wall and slightly decreases around the wall curvature and that is due to the decrease of the tube diameter till it reaches the normal one of the non-deformed part of the wall.

To understand more the flow behavior in the given flow domain, the effect of various geometrical and fluid parameters on the flow is studied, namely, the Reynolds number (Re), the curvature length (L_0) and the curvature max-

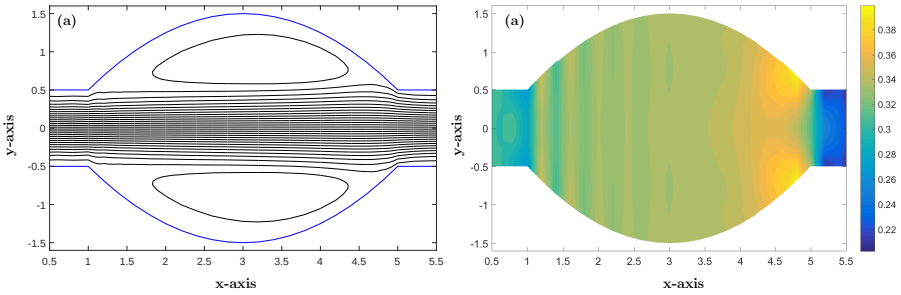

Fig. 13: Streamlines profile (a) and pressure contours (b) obtained in the steady regime for the case 1b

imum height (ϵ). The effect of the Reynolds variation on the flow is shown in Figure 9 at $t = 10$. The same values given in Table 4 are kept for the other parameters and different Reynolds numbers $Re \in \{100,\ 200,\ 300\}$ are chosen. It is observed that the roll's appearance becomes clearer and it takes place in a large zone when the Reynolds number is increased.

The same analysis was made to clarify the effect of the curvature length L_0. The obtained flow streamlines were presented at $t = 10$ and for values of L_0 varying in $\{3,\ 4,\ 5\}$. The other parameters values are fixed and given in Table 4. It can be clearly observed that for an increase in L_0, the rolls become larger and take more time to reach the steady regime due to the increase in the deformed zone. Finally, the influence of the curvature maximum height on the flow at $t = 10$ is analyzed. The resulting streamlines for various values of ϵ, $\epsilon \in \{0.5,\ 1,\ 1.5\}$, are presented in Figure 11. It is demonstrated that small values of ϵ result in a uniform flow while an increase in the value of ϵ results on a large number of rolls. This is due to the large zone for the rolls to take place and to expand.

Case 1b : Symmetrical two wall curvatures

In this case, the behavior of the flow with the presence of two symmetrical curvatures on the two sides of the channel walls is investigated. The considered wall geometry with the presence of two symmetrical curvatures is shown in Fig 6a. Several numerical tests have been made with a fixed wall and steady inlet flow using the same curve function defined in Eq. (52) for both upper and lower sides of the wall and with the same structural values for both sides. The no-slip condition is assumed on the rigid wall and the inlet function, without the unsteady part, is defined as follows

$$u_{in} = \left[1 - \left(\frac{y}{R}\right)^2\right] \tag{54}$$

The geometric and mesh parameters, used in Case 1b, are the same ones given in Table 3. The curvature is supposed to be symmetrical for both sides of the wall and the structural and fluid parameters are given in Table 4. The

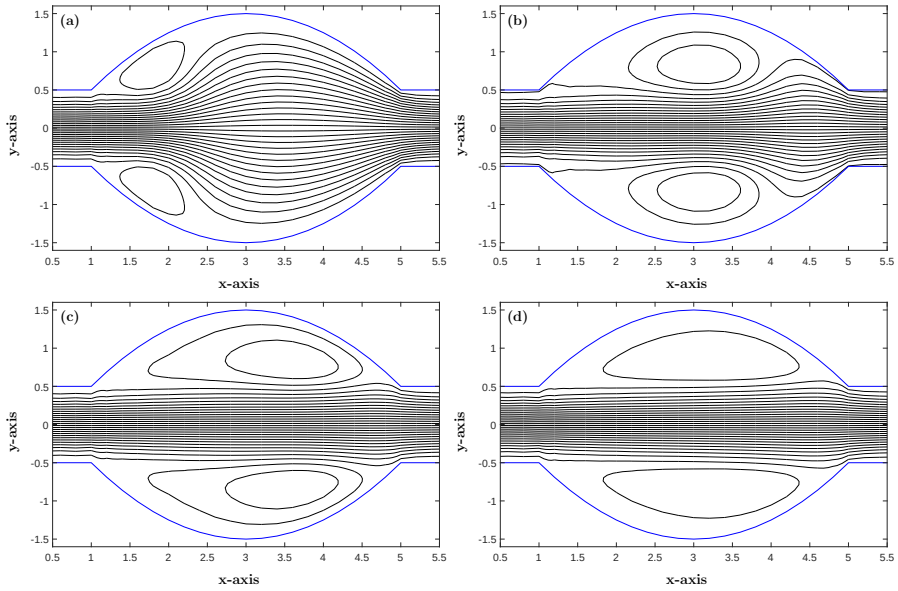

Fig. 14: Flow evolution over time for the Case 1b : (a) $t = 5$, (b) $t = 9$, (c) $t = 13$, (d) $t = 25$.

results were obtained using the same mesh parameters and time step as in Case 1a.

Figure 13 shows the streamlined profiles and pressure contours in the steady regime for the given values of the geometrical, structural and fluid parameters values in Tables 3-4. It can be observed from Figure 13a, as in the first case, that the flow is uniform in the inlet and middle of the tube, while near the curved part of each side of the wall the flow forms symmetrical rolls on both sides of the channel covering the whole deformed zones. Similarly, Figure 13b shows a higher pressure occurring near the ends of the symmetrical curvatures that slightly decreases around the deformed part of the wall toward the inlet of the tube.

Figures 14-15 represent the streamline profiles and pressure contours evolution over time for fixed values of structural and fluid parameters given in Table 4. Figure 14 presents the streamlines for the time values $t \in \{5,\ 9,\ 13,\ 25\}$. It is observed that the fluid begins to form rolls on both curved sides of the walls in a symmetrical way and starts to develop over time in that zone of the tube and keeps taking more space till filling the full deformed zone of the tube. That is due to the increase of the fluid velocity until the flow reaches the steady regime.

The pressure evolution over time in the case of two symmetrical curvatures on both sides of the channel is presented in Figure 15. The pressure contours are obtained for $t \in \{5,\ 10,\ 14.7,\ 25\}$ and for the same fixed values of the structural and fluid parameters given in Table 4. A higher pressure occurs

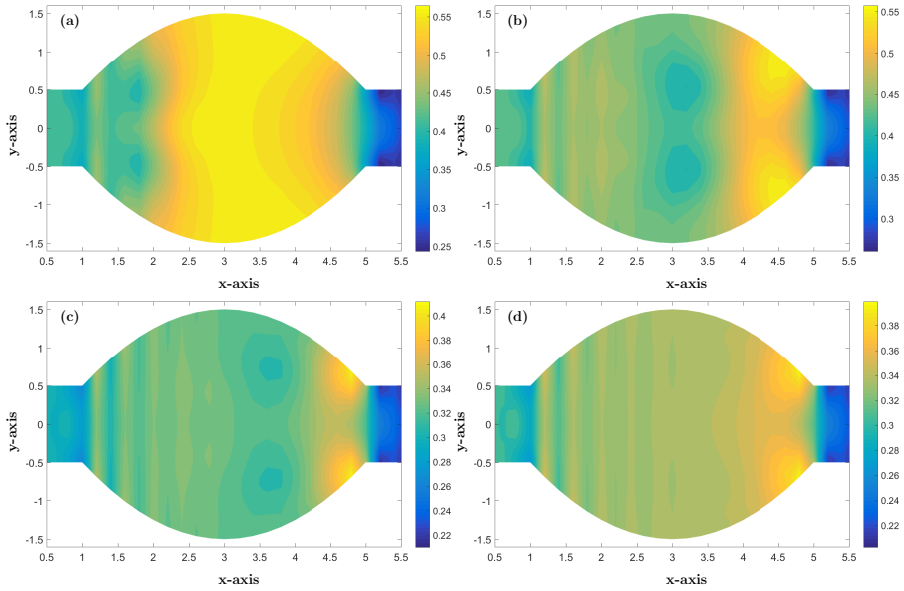

Fig. 15: Pressure contours over time for the Case 1b : (a) $t = 5$, (b) $t = 9$, (c) $t = 13$, (d) $t = 25$.

near the middle of both curvatures and continues to move around them in a symmetrical way heading to both ends of the deformed walls till it reaches a steady regime. The pressure then takes a higher value near the ends of the deformed walls and slightly decreases around the wall curvatures. That is due to the decrease in the tube diameter till reaching the normal one of the non-deformed parts of the walls.

While comparing these results to the one side curvature case, 1a, it is noticed that the fluid finds more space to take place in this case because of the new symmetrical deformed side. Thus, the fluid rolls occur less larger in case 1b than 1a while using the same fluid parameters given in Table 4. Also, the highest pressure value in this sub-case is lower than in the previous one.

Case 1c : Asymmetrical wall curvatures

In this final sub-case, the assumption of a steady inlet velocity is kept and the flow behavior in a channel with two non-symmetrical curvatures of the wall to observe the effect of the asymmetry on the fluid flow is investigated. The considered flow domain with asymmetrical curvatures is sketched in Figure 6b. As previously done, numerical tests with the consideration of a fixed wall and steady inlet flow are elaborated using the same curve function defined in Eq. (52), for both upper and lower sides of the wall. Different structural parameters values are used to consider better the non-symmetry of the walls geometries. Again, on the rigid wall, the no-slip condition is taken and the inlet function u_{in} is used as in the previous sub-case, 1b, given in Eq. (54).

Table 5: Structural parameters for the lower side of the wall for the Case 1c and the Case 2.

Parameters	Values
Aneurysm location d_{down}	2.5
Aneurysm length $L_{0,down}$	3
aneurysm max. height ϵ_{down}	0.9

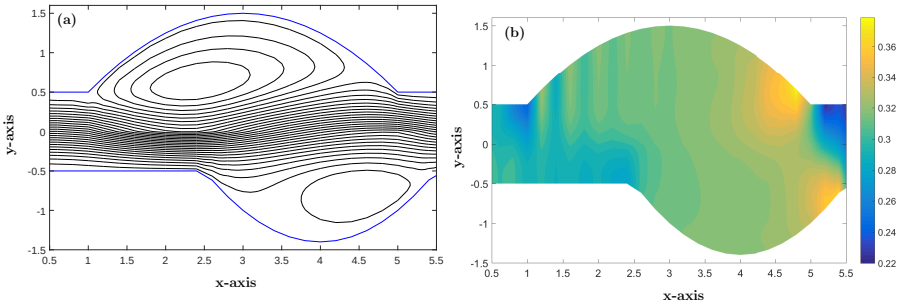

Fig. 16: Streamlines profiles (a) and pressure contours (b) obtained in the steady regime for asymmetrical curvatures

The geometric and mesh parameters, used in this sub-case, are the same ones given in Table 3. As the curvatures are supposed to be non-symmetric, the structural parameters used for the upper side of the wall and fluid parameters are taken from Table 4 while the lower side structural parameters are defined in Table 5. The numerical results were obtained using the same mesh parameters and time step as in the other sub-cases.

Figure 16 shows the steady solution obtained for the streamlined profiles and pressure contours in the steady regime for the geometrical, structural and fluid parameters values given in Tables 3-5. It is observed from Figure 16a that the flow is uniform in the inlet and quasi-uniform in the middle of the tube. Near the curved part of each side of the wall, the flow forms non-symmetrical rolls in the two sides of the channel covering the whole deformed zone on the upper side, while on the lower side the rolls take place in the right part of the deformed zone. The same observation goes to the pressure contours plotted in Figure 16b that shows a higher pressure near the end of both non-symmetrical curvatures that slightly decreases around the deformed part of the wall toward the inlet of the tube. The pressure is lower at the end of the lower curvature than in the upper one.

With respect to time, the streamline profiles and pressure contours evolution for fixed values of structural and fluid parameters given in Tables 4-5 are presented in Figures 17-18. Figure 17 represents the streamlines for the time values $t \in \{5,\ 9,\ 13,\ 25\}$ showing that the fluid starts to form rolls in the upper curvature of the tube and takes some time for the lower curvature, this is due to the distance between the two curvatures and the asymmetrical pro-

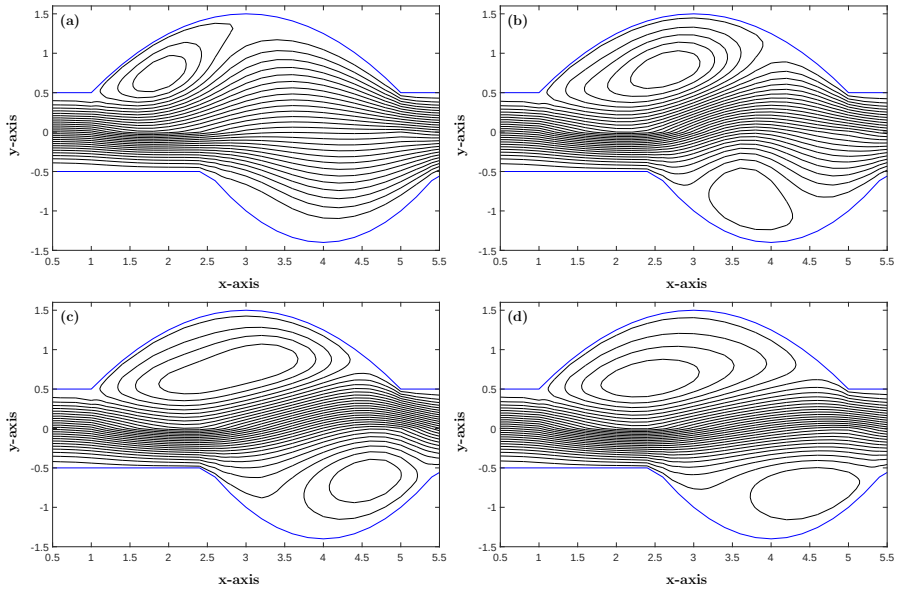

Fig. 17: Flow evolution over time for Case 1c : (a) $t = 5$, (b) $t = 9$, (c) $t = 13$, (d) $t = 25$.

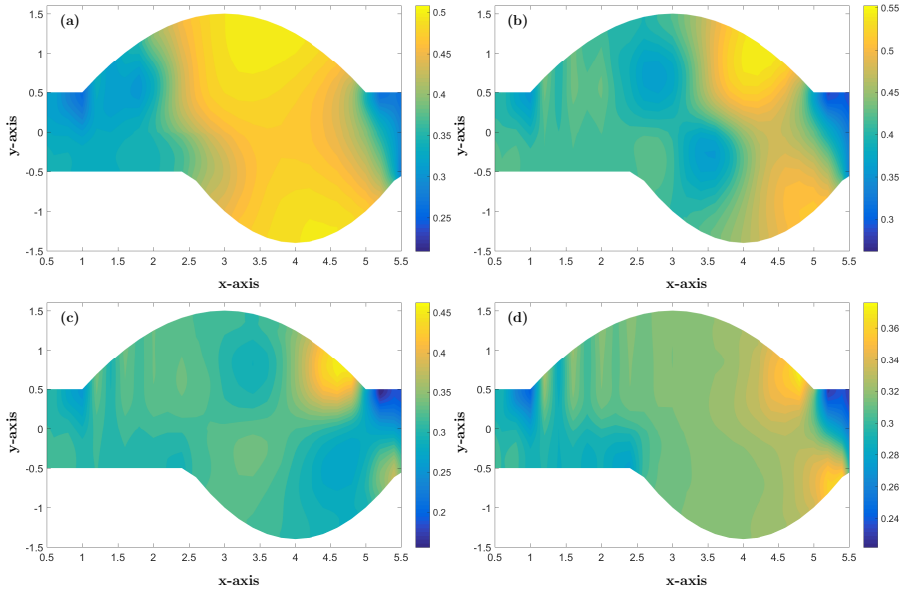

Fig. 18: Pressure contours over time for Case 1c : (a) $t = 5$, (b) $t = 9$, (c) $t = 13$, (d) $t = 25$.

prieties until the steady regime is reached where the rolls fill the full deformed zone of the upper side of tube and doesn't fill all the space in the lower side that is due to the asymmetrical positions of the curvatures and to the fact that the fluid found more space at the starting position of the lower curvature.

Figure 18 presents the pressure evolution over time in the case of two non-symmetrical curvatures on the two sides of the channel. The same proprieties as in Figure 17 are used. New observations are made that differ from the ones obtained in other sub-cases. Higher pressure occurs near the middle of the curvatures in a non-symmetrical way and continue to move around the curvatures in a non-symmetrical way heading to both ends of the deformed walls till reaching the steady regime where the pressure takes a higher value near the ends of the deformed walls and slightly decreases around the wall curvatures. That is due to the decrease of the tube diameter, while it is remarked that the pressure value at the end of the upper curvature is higher than in the end of the lower curvature due to the non-symmetrical proprieties of the curvatures.

Comparison with the previous sub-cases, 1a and 1b, it can be noticed that, as in Case 1b, the two sides curvatures offer more space to the fluid. The non-symmetrical effect on the fluid flow is clearly shown in the resulting figures where the rolls are not symmetrical and have less appearance in the lower curvature than in the upper one. The pressure contours also display a non-symmetrical behavior on the non-symmetrical walls.

4.2.2 Case 2 : Rigid wall with pulsatile inlet

In this case, the flow behavior is studied in a fixed geometry with the assumption of a pulsatile inlet velocity profile. The asymmetric wall geometry presented in Figure 6b is considered herein. As in the previous cases, several numerical tests with the consideration of a fixed wall and pulsatile inlet flow are performed on the rigid wall, as a boundary condition, the no-slip condition is assumed. Also, the steady solution, found in Case 1, is used as an initial condition in order to better understand the pulsation effect on the flow. The pulsatile inlet function is defined as follows

$$u_{in}(y,t) = u_0(t)\left[1 - \left(\frac{y}{R}\right)^2\right] \tag{55}$$

where the function $u_0(t)$ involved in the inlet flow is a periodic function that presents the velocity amplitude variation in the x-axis direction over time, as shown in Figure 19a. For a proper understanding of the fluid flow in the proposed domain, the set of selected time values where the streamlines and pressure contours are plotted and presented in Figure 19b.

The geometric and mesh parameters used in Case 2 are also given in Table 3. The structural parameters used for the upper side of the wall and fluid parameters are taken from Table 4 while the lower side structural parameters are defined in Table 5. The numerical results were obtained using the same mesh parameters and time step as in Case 1.

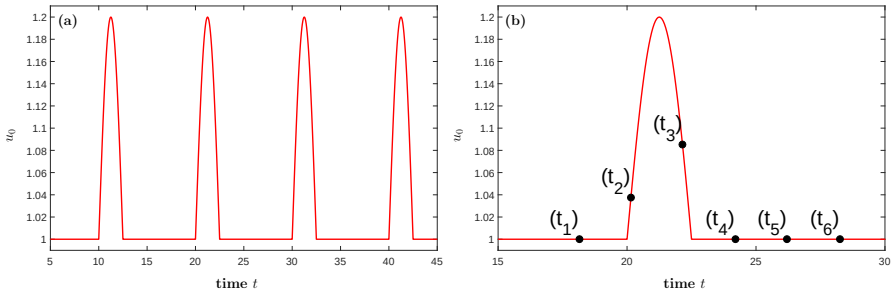

Fig. 19: Amplitude of the inlet velocity as a function of time (a) with zoom in of one single pulse with the set of time samples (b)

Figures 20-21 show the streamlines profiles and pressure contours evolution with respect to the set of time values defined in Figure 19b with fixed geometrical, structural and fluid parameters values given in Tables 3-5. The main obtained results are: the flow becomes periodic due to the periodic inlet velocity, an increase in the inlet velocity results in the expansion of fluid rolls in both curvatures in a non-symmetrical way, and when it decreases, the rolls become less visible and maybe removed in the lower curvature zone. Also, the flow keeps it uniform behavior in the inlet and quasi-uniform in the middle of the tube as in the previous case. The same observations are made for the pressure contours, as obtained in previous case. Higher pressure occurs near the end of the non-symmetrical curvatures and slightly decreases around the deformed part of the wall toward the inlet of the tube.

In comparison with the steady inlet case, it is clearly noticeable that the pulsation effect on the fluid flow behavior. An interesting result of the pulsatile flow is that there is a time difference between the instant where the inlet amplitude reaches its maximum value and the instant where the maximum appearance of the fluid rolls occurs.

It is important to mention that the previous results are well validated with the existing ones from the literature and other numerical techniques.

4.3 FSI model for pulsatile blood flow with elastic asymmetric aneurysm

In this subsection, some interesting results are obtained and analyzed from the simulation of the fluid-tube interaction model using the coupled numerical scheme presented in this paper. In this case, the structure walls are assumed not fully rigid and consist of an elastic part. The fluid and structure behaviors were studied for pulsatile inlet velocity and for non-symmetrical walls of the channel.

As the main application, the pulsatile blood flow in asymmetric elastic arterial aneurysm is considered. A two dimensional geometry defined by a tube with both rigid and elastic parts of the wall, as previously shown in

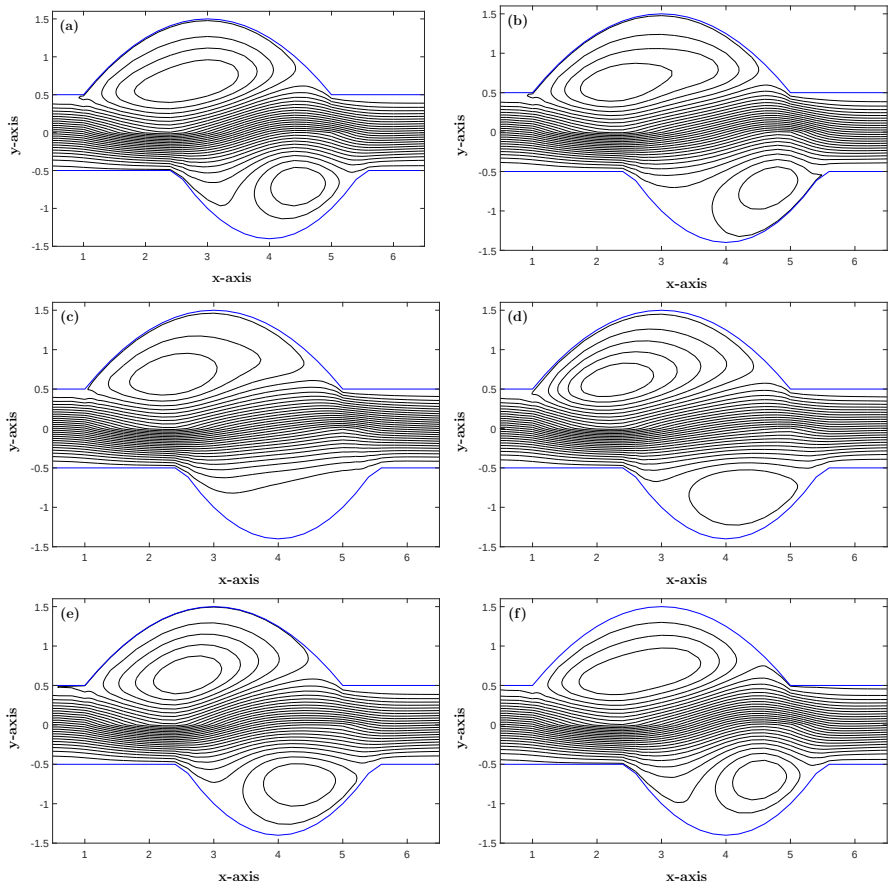

Fig. 20: Flow evolution over time for the Case 2 : (a) $t = 18$, (b) $t = 20$, (c) $t = 22$, (d) $t = 24$, (e) $t = 28$, (f) $t = 28$.

Figure 1 is used. Based on the FSI algorithm, several numerical tests have been made to simulate the fluid-tube interaction with pulsatile inlet velocity and asymmetrical elastic parts of the tube walls. The no-slip condition is considered at the rigid part of the wall and the continuity of the velocity at the elastic part, as defined in (28). The pulsatile inlet function is defined as follows

$$u_{in}(y,t) = u_0(t)\left[1 - \left(\frac{y}{R}\right)^2\right] \tag{56}$$

where the function $u_0(t)$ is the inlet velocity amplitude. For a proper understanding of the fluid flow in the proposed domain, the set of selected time values is presented in Figure 22 where the streamlines and pressure contours were taken.

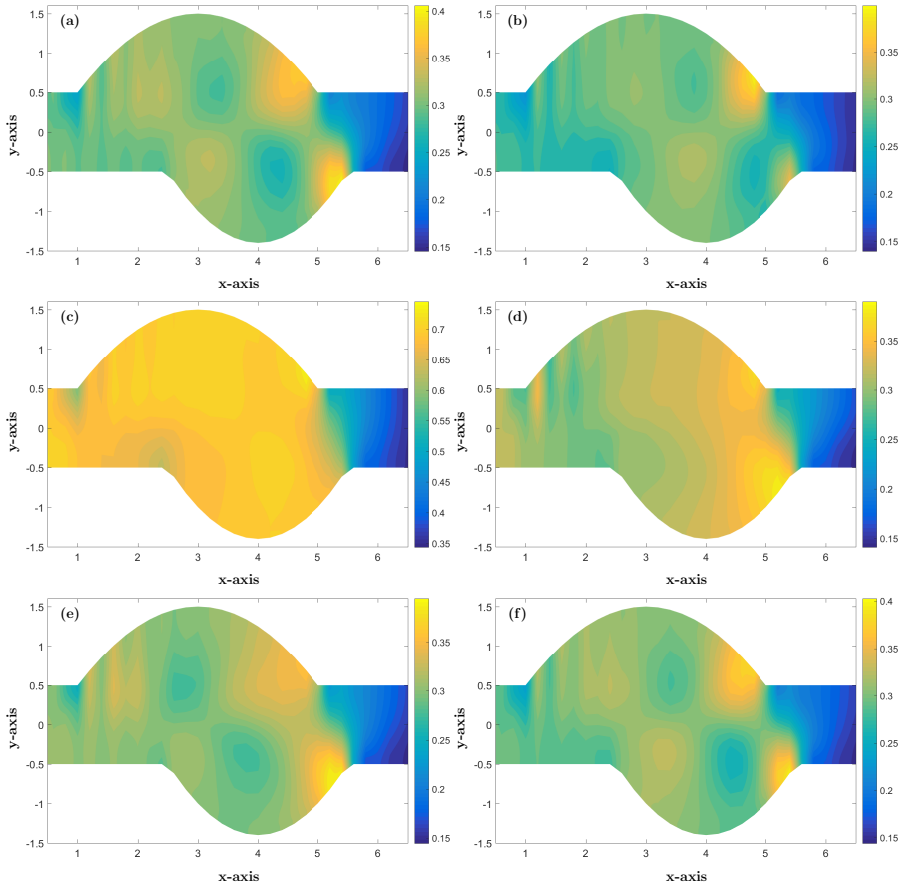

Fig. 21: Pressure contours over time for the Case 2 : (a) $t = 18$, (b) $t = 20$, (c) $t = 22$, (d) $t = 24$, (e) $t = 28$, (f) $t = 28$.

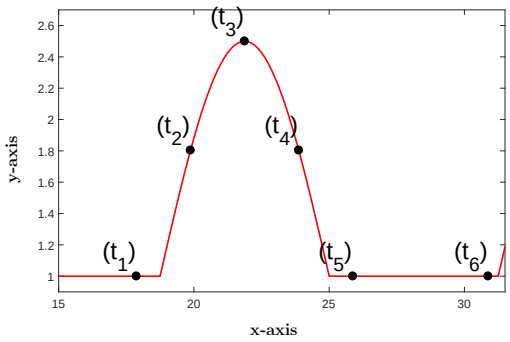

Fig. 22: The set of time samples for the Case 3

Table 6: Geometric parameters used in case 1.

Parameters	Values	Parameters	Values
Initial time t_0	0	Final time T	50
Time step Δt	0.1250	Normal Radius $R0$	0.5
Length of the channel L	10	Number of nodes ($Nx \times Ny$)	5151
x-Space step Δx	0.1	y-Space step Δy	0.02

Table 7: Fluid & structural parameters for both aneurysm sides.

Parameters	Values	Parameters	Values
Reynolds number Re	200	h	0.05
μ_s	1000	λ_s	1000
p_0	15	P_ext	5
Upper Aneurysm location d_{up}	1	Lower Aneurysm location d_{down}	2.5
Upper Aneurysm length $L_{0,up}$	4	Lower Aneurysm length $L_{0,down}$	3

The geometrical and mesh parameters used in the considered FSI problem are given in Table 6, while the structural parameters used for the upper and lower sides of the wall and fluid parameters are given in Table 7. The results were obtained using a regular grid, with 101×51 fluid and pressure nodes. The time step used in these numerical tests is $\Delta t = 0.1250$. During the computation process, no stability problems is seen, or in the obtained solutions.

Figures 23-24 show the streamlines profiles and pressure contours evolution with respect to the set of time values defined in Figure 22 with fixed values of the geometrical, structural and fluid parameters values presented in Tables 6-7. It is clearly demonstrated that the behavior of the fluid flow is not the same as discussed in the previous cases. The flow becomes periodic due to the pulsatile inlet velocity and the clear effect on the rolls in both curvature zones is presented. On the other hand, a clear change is observed in the elastic walls displacement over time due to the fluid-tube interaction in a periodic way. Also, when the velocity increases at the inlet, the rolls become less clear and start to expand over time. As for the pressure contours, it is clearly shown that a higher pressure occurs near the end of both non-symmetrical curvatures and increases as the inlet velocity increases and starts to take its initial values over time. The pressure evolution near the tube wall plays a rule in the displacement variation of the upper and lower elastic parts.

Figure 25 shows the upper and lower maximum and minimum displacements of the elastic parts in the selected time values. It is clearly observed that there is an effect of the inlet pulsation on the wall deformation and there is a time difference between the instant where the inlet velocity reaches its maximum. The maximum wall displacement takes place on both the upper and lower sides of the tube walls. The wall displacements and flow behavior are in good agreement with previous research works in [46, 40, 47].

With comparison to the rigid case, a different behavior of the streamlines-pressure profiles due to the increase and decrease in both deformations of the elastic walls. It is observed that the rolls get infected and become less

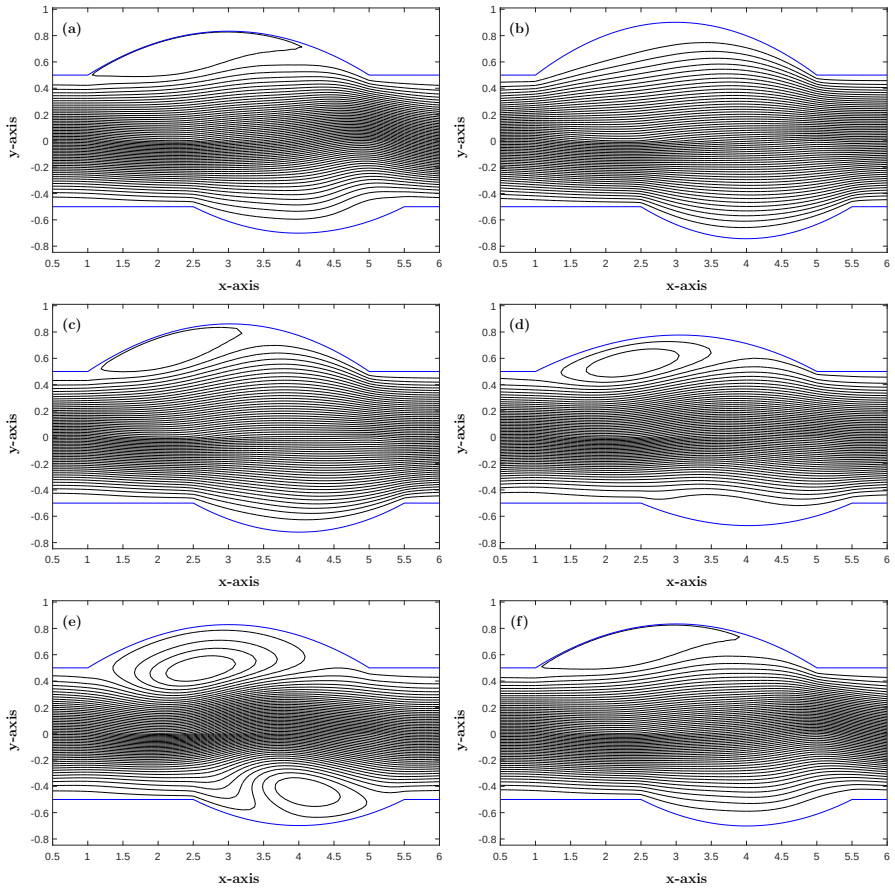

Fig. 23: Flow evolution over time for the FSI problem : (a) $t = 18$, (b) $t = 20$, (c) $t = 22$, (d) $t = 24$, (e) $t = 26$, (f) $t = 31$.

visible when there is an increase in the aneurysm displacement and that gives more space for the fluid to take place. For the pressure variation, it is clearly observed that the effect of the pressure on the wall displacement as it takes maximum form when the pressure reaches its maximum value near the wall and the minimum displacement appears when the pressure takes its lowest value near the elastic walls.

5 Conclusion

This paper presents a mathematical modeling and numerical simulation for fluid-tube interaction problems using large deformation theory. The application is mainly in cardiovascular systems and particularly abdominal deformed arteries and arterial aneurysms. An FSI model has been elaborated to describe

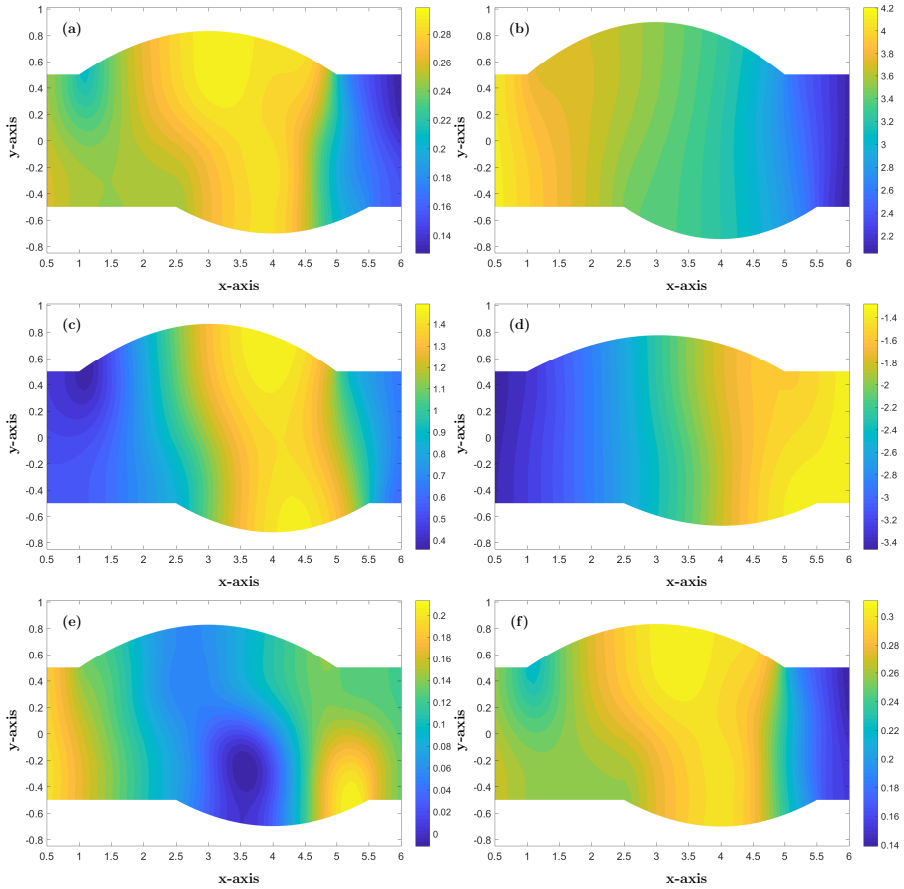

Fig. 24: Pressure contours over time for the FSI problem : (a) $t = 18$, (b) $t = 20$, (c) $t = 22$, (d) $t = 24$, (e) $t = 26$, (f) $t = 31$.

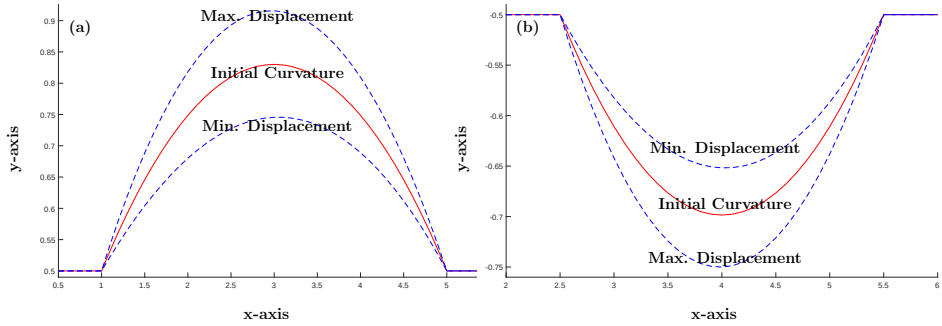

Fig. 25: Maximum and minimum wall displacements during a single pulse of the upper (a) and lower (b) aneurysm sides with respect to the initial curvature

incompressible fluid flow behavior in deformable geometries. This model is based on a simplified non-linear system of equations that are derived to describe the wall dynamics in a large deformation domain coupled with the non-linear Navier-Stokes equations. The pulsatile fluid flow through an elastic tube with non-symmetrical wall geometries is investigated.

Efficient mathematical algorithms and numerical simulations are elaborated based on the splitting finite difference method and shooting procedure. A well-adopted semi-implicit and predictor-correction methods are elaborated. A mesh transformation is used to account for irregular domains. The coupled nonlinear fluid-structure interaction problem is numerically solved and the wall displacement and fluid velocity-pressure field are computed. Numerical experiments in three different cases have been investigated to fully understand flow behavior in rigid curved tubes and tubes with non-symmetrical elastic parts. The effects of several structural and fluid parameters on flow are studied and discussed.

The obtained results for different structural and fluid settings of the proposed model are presented. The main observations are summarized as follow

- The structural and fluid solver are validated and adapted to the presented model for the elastic aneurysm motion and blood flow behavior.
- For the case of rigid deformed walls and steady inlet velocity, the flow behavior changes when changing the wall curvatures parameters or with the Reynolds number. The streamline profiles, in the case of non-symmetrical walls, behave in a non-symmetrical way, as the rolls are not symmetrical and have less appearance in the lower curvature than in the upper one. The same observations are made for the pressure contours compared to other cases of one or two symmetrical curvatures.
- For the case of two rigid non-symmetrical curvatures with a periodic pulsatile inlet velocity, it is clearly noticeable that the fluid flow behavior appears to be periodic. Also , there is a gap or a time difference between the instant where the inlet amplitude reaches its maximum value and the instant where the maximum appearance of the fluid rolls occurs in both curvatures zones.
- For the FSI model, the case of two non-symmetric elastic curvature with a pulsatile inlet velocity, the pulsation affects the elastic walls displacements and appears to be periodic with a time gap between when the inlet amplitude reaches its maximum value and when the maximum wall displacement of the elastic walls takes place.
- Also, for the case of deformed walls, it is observed that the rolls in the deformed zone become less visible due to the increase in the wall displacement and start to build up in a non-symmetrical way over time with clear appearence in the upper aneurysm than in the lower one till it reaches the initial form.
- A large variation of the wall displacement with respect to the pressure values near the elastic walls is clearly demonstrated.
- The results are in good agreement with previous research work.

The presented fluid-tube interaction model may be very useful in predicting and diagnosing many cardiovascular diseases such as arterial aneurysms and abnormally deformed arteries. The model can be further investigated for higher dimensions and different fluid rheology, as blood is often considered as a non-Newtonian fluid.

Acknowledgements The authors would like to acknowledge the financial support of the CNRST and the Moroccan Ministry of Higher Education and Scientific Research with the project PPR2/06/2016. The authors acknowledge with thanks the technical and financial supports from PPR2.

References

1. H.-J. Bungartz and M. Schäfer, eds., *Fluid-Structure Interaction*, vol. 53 of *Lecture Notes in Computational Science and Engineering*. Berlin, Heidelberg: Springer Berlin Heidelberg, 2006.
2. P.-N. Sun, D. Le Touzé, G. Oger, and A.-M. Zhang, "An accurate fsi-sph modeling of challenging fluid-structure interaction problems in two and three dimensions," *Ocean Engineering*, vol. 221, p. 108552, 2021.
3. A. Khayyer, Y. Shimizu, H. Gotoh, and K. Nagashima, "A coupled incompressible sph-hamiltonian sph solver for hydroelastic fsi corresponding to composite structures," *Applied Mathematical Modelling*, vol. 94, pp. 242–271, 2021.
4. J. Zimmermann, K. Bäumler, M. Loecher, T. E. Cork, F. O. Kolawole, K. Gifford, A. L. Marsden, D. Fleischmann, and D. B. Ennis, "Quantitative hemodynamics in aortic dissection: Comparing in vitro mri with fsi simulation in a compliant model," in *Functional Imaging and Modeling of the Heart* (D. B. Ennis, L. E. Perotti, and V. Y. Wang, eds.), (Cham), pp. 575–586, Springer International Publishing, 2021.
5. C. Alberto Figueroa, S. Baek, C. A. Taylor, and J. D. Humphrey, "A computational framework for fluid-solid-growth modeling in cardiovascular simulations," *Computer Methods in Applied Mechanics and Engineering*, vol. 198, pp. 3583–3602, sep 2009.
6. S. Frei, T. Richter, and T. Wick, "Long-term simulation of large deformation, mechano-chemical fluid-structure interactions in ALE and fully Eulerian coordinates," *Journal of Computational Physics*, vol. 321, pp. 874–891, sep 2016.
7. J. T. McPhee, J. S. Hill, and M. H. Eslami, "The impact of gender on presentation, therapy, and mortality of abdominal aortic aneurysm in the United States, 2001-2004," *Journal of Vascular Surgery*, vol. 45, pp. 891–899, may 2007.
8. S. Aggarwal, A. Qamar, V. Sharma, and A. Sharma, "Abdominal aortic aneurysm: A comprehensive review," *Experimental and Clinical Cardiology*, vol. 16, no. 1, pp. 11–15, 2011.
9. R. A. Peattie, T. J. Riehle, and E. I. Bluth, "Pulsatile Flow in Fusiform Models of Abdominal Aortic Aneurysms: Flow Fields, Velocity Patterns and Flow-Induced Wall Stresses," *Journal of Biomechanical Engineering*, vol. 126, p. 438, aug 2004.
10. D. Roy, C. Kauffmann, S. Delorme, S. Lerouge, G. Cloutier, and G. Soulez, "A literature review of the numerical analysis of abdominal aortic aneurysms treated with endovascular stent grafts," *Computational and Mathematical Methods in Medicine*, vol. 2012, pp. 1–16, sep 2012.
11. Y. Li, Z. Ji, L. Yang, P. Zhang, B. Xu, and J. Zhang, "Thermal-fluid-structure coupling analysis for valve plate friction pair of axial piston pump in electrohydrostatic actuator (EHA) of aircraft," *Applied Mathematical Modelling*, vol. 47, pp. 839–858, jul 2017.
12. D. Kamensky, M. C. Hsu, D. Schillinger, J. A. Evans, A. Aggarwal, Y. Bazilevs, M. S. Sacks, and T. J. Hughes, "An immersogeometric variational framework for fluid-structure interaction: Application to bioprosthetic heart valves," *Computer Methods in Applied Mechanics and Engineering*, vol. 284, pp. 1005–1053, feb 2015.

13. J. ye Gan, H. S. Im, X. ying Chen, G. C. Zha, and C. L. Pasiliao, "Delayed detached Eddy simulation of wing flutter boundary using high order schemes," *Journal of Fluids and Structures*, vol. 71, pp. 199–216, may 2017.
14. C. Graczykowski, "Mathematical models and numerical methods for the simulation of adaptive inflatable structures for impact absorption," *Computers and Structures*, vol. 174, pp. 3–20, oct 2016.
15. J. Yan, A. Korobenko, X. Deng, and Y. Bazilevs, "Computational free-surface fluid-structure interaction with application to floating offshore wind turbines," *Computers and Fluids*, vol. 141, pp. 155–174, dec 2016.
16. F. Piatti, F. Sturla, G. Marom, J. Sheriff, T. E. Claiborne, M. J. Slepian, A. Redaelli, and D. Bluestein, "Hemodynamic and thrombogenic analysis of a trileaflet polymeric valve using a fluid-structure interaction approach," *Journal of Biomechanics*, vol. 48, pp. 3650–3658, oct 2015.
17. C. Chiastra, F. Migliavacca, M. Á. Martínez, and M. Malvè, "On the necessity of modelling fluid-structure interaction for stented coronary arteries," *Journal of the Mechanical Behavior of Biomedical Materials*, vol. 34, pp. 217–230, jun 2014.
18. G. B. Kalyana Sundaram, K. R. Balakrishnan, and R. K. Kumar, "Aortic valve dynamics using a fluid structure interaction model - The physiology of opening and closing," *Journal of Biomechanics*, vol. 48, pp. 1737–1744, jul 2015.
19. L. S. Pan, T. Y. Ng, G. R. Liu, K. Y. Lam, and T. Y. Jiang, "Analytical solutions for the dynamic analysis of a valveless micropump - A fluid-membrane coupling study," *Sensors and Actuators, A: Physical*, vol. 93, pp. 173–181, sep 2001.
20. M. Turkyilmazoglu, "Air blast response of compaction foam having a deformable front face panel incorporating fluid structure interactions," *International Journal of Mechanical Sciences*, vol. 105, pp. 340–347, jan 2016.
21. F. Sotiropoulos and X. Yang, "Immersed boundary methods for simulating fluid-structure interaction," *Progress in Aerospace Sciences*, vol. 65, pp. 1–21, feb 2014.
22. G. H. Cottet and E. Maitre, "A semi-implicit level set method for multiphase flows and fluid-structure interaction problems," *Journal of Computational Physics*, vol. 314, pp. 80–92, jun 2016.
23. S. Miyauchi, S. Takeuchi, and T. Kajishima, "A numerical method for interaction problems between fluid and membranes with arbitrary permeability for fluid," *Journal of Computational Physics*, vol. 345, pp. 33–57, sep 2017.
24. F. B. Tian, H. Dai, H. Luo, J. F. Doyle, and B. Rousseau, "Fluid-structure interaction involving large deformations: 3D simulations and applications to biological systems," *Journal of Computational Physics*, vol. 258, pp. 451–469, feb 2014.
25. J. De Hart, G. W. M. Peters, P. J. G. Schreurs, and F. P. T. Baaijens, "A two-dimensional fluid-structure interaction model of the aortic value," *Journal of Biomechanics*, vol. 33, pp. 1079–1088, sep 2000.
26. K. J. Paik and P. M. Carrica, "Fluid-structure interaction for an elastic structure interacting with free surface in a rolling tank," *Ocean Engineering*, vol. 84, pp. 201–212, jul 2014.
27. J. Kumar and F. H. Wurm, "Bi-directional fluid-structure interaction for large deformation of layered composite propeller blades," *Journal of Fluids and Structures*, vol. 57, pp. 32–48, aug 2015.
28. H. Bakhti and L. Azrar, "Steady Flow of Couple-Stress Fluid in Constricted Tapered Artery: Effects of Transverse Magnetic Field, Moving Catheter, and Slip Velocity," *Journal of Applied Mathematics*, vol. 2016, pp. 1–11, 2016.
29. H. Bakhti, L. Azrar, and D. Baleanu, "Pulsatile blood flow in constricted tapered artery using a variable-order fractional Oldroyd-B model," *Thermal Science*, vol. 21, no. 1, pp. 29–40, 2017.
30. E. A. Finol and C. H. Amon, "Blood Flow in Abdominal Aortic Aneurysms: Pulsatile Flow Hemodynamics," *Journal of Biomechanical Engineering*, vol. 123, p. 474, oct 2001.
31. E. A. Finol, K. Keyhani, and C. H. Amon, "The Effect of Asymmetry in Abdominal Aortic Aneurysms Under Physiologically Realistic Pulsatile Flow Conditions," *Journal of Biomechanical Engineering*, vol. 125, p. 207, apr 2003.
32. M. G. Rabby, S. P. Shupti, and M. M. Molla, "Pulsatile non-newtonian laminar blood flows through arterial double stenoses," *Journal of Fluids*, vol. 2014, pp. 1–13, 5 2014.

33. P. Reorowicz, D. Obidowski, P. Klosinski, W. Szubert, L. Stefanczyk, and K. Jozwik, "Numerical simulations of the blood flow in the patient-specific arterial cerebral circle region," *Journal of Biomechanics*, vol. 47, pp. 1642–1651, may 2014.
34. M. G. Rabby, R. Sultana, S. P. Shupti, and M. M. Molla, "Laminar blood flow through a model of arterial stenosis with oscillating wall," *International Journal of Fluid Mechanics Research*, vol. 41, pp. 417–429, 2014.
35. A. J. Apostolidis, A. P. Moyer, and A. N. Beris, "Non-Newtonian effects in simulations of coronary arterial blood flow," *Journal of Non-Newtonian Fluid Mechanics*, vol. 233, pp. 155–165, jul 2015.
36. S. P. Shupti, M. G. Rabby, and M. M. Molla, "Rheological behavior of physiological pulsatile flow through a model arterial stenosis with moving wall," *Journal of Fluids*, vol. 2015, pp. 1–22, 6 2015.
37. Y. Imai, T. Omori, Y. Shimogonya, T. Yamaguchi, and T. Ishikawa, "Numerical methods for simulating blood flow at macro, micro, and multi scales," *Journal of Biomechanics*, vol. 49, pp. 2221–2228, jul 2016.
38. S. P. Shupti, M. M. Molla, and M. Mia, "Pulsatile non-newtonian fluid flows in a model aneurysm with oscillating wall," *Frontiers in Mechanical Engineering*, vol. 3, p. 12, 11 2017.
39. R. A. Peattie, T. J. Riehle, and E. I. Bluth, "Pulsatile Flow in Fusiform Models of Abdominal Aortic Aneurysms: Flow Fields, Velocity Patterns and Flow-Induced Wall Stresses," *Journal of Biomechanical Engineering*, vol. 126, p. 438, aug 2004.
40. M. Hamadiche, "Numerical simulation and mathematical analysis of flow-wall interaction in the large deformation application to the dynamics of the aneurysms," *Journal of Thermal Engineering*, vol. 1, p. 42, jan 2015.
41. G. Guidoboni, R. Glowinski, N. Cavallini, and S. Canic, "Stable loosely-coupled-type algorithm for fluid-structure interaction in blood flow," *Journal of Computational Physics*, vol. 228, pp. 6916–6937, oct 2009.
42. G. Guidoboni, R. Glowinski, N. Cavallini, S. Canic, and S. Lapin, "A kinematically coupled time-splitting scheme for fluid-structure interaction in blood flow," *Applied Mathematics Letters*, vol. 22, pp. 684–688, may 2009.
43. M. Bukač, S. Čanić, R. Glowinski, J. Tambača, and A. Quaini, "Fluid-structure interaction in blood flow capturing non-zero longitudinal structure displacement," *Journal of Computational Physics*, vol. 235, pp. 515–541, feb 2013.
44. M. A. Fernández, J. F. Gerbeau, and C. Grandmont, "A projection semi-implicit scheme for the coupling of an elastic structure with an incompressible fluid," *International Journal for Numerical Methods in Engineering*, vol. 69, pp. 794–821, jan 2007.
45. L. Formaggia, A. Moura, and F. Nobile, "On the stability of the coupling of 3D and 1D fluid-structure interaction models for blood flow simulations," *ESAIM: Mathematical Modelling and Numerical Analysis*, vol. 41, pp. 743–769, jul 2007.
46. M. Hamadiche, "Aneurysm no-linear unsteady dynamic: Mathematical modeling," *American Society of Mechanical Engineers, Pressure Vessels and Piping Division (Publication) PVP*, vol. 4, 1 2014.
47. H. Bakhti, S. Azoug, and L. Azrar, "Blood flow simulation through two-dimensional complex stenosed arteries using viscoelastic oldroyd-b fluid," pp. 1–4, IEEE, 12 2019.